

---

## Repeated fluid expulsions during events of rapid sea-level rise in the Gulf of Lion, western Mediterranean Sea.

Gay Aurelien <sup>1,\*</sup>, Cavailhes Thibault <sup>2</sup>, Grauls Dominique <sup>3</sup>, Marsset Bruno <sup>4</sup>, Marsset Tania <sup>5</sup>

<sup>1</sup> Géosciences Montpellier, Université de Montpellier 2, Place Eugène Bataillon, 34095 Montpellier, France

<sup>2</sup> EPOC, Université de Bordeaux, Site de Talence, 33615 Pessac, France

<sup>3</sup> Consulting , 9 rue O'Quin 64000, Pau, France

<sup>4</sup> IFREMER-EDROME, Géosciences Marines, 29280, Plouzané, France

<sup>5</sup> IFREMER, Géosciences Marines, 29280, Plouzané, France

\* Corresponding author : Aurélien Gay, email address : [aurelien.gay@gm.univ-montp2.fr](mailto:aurelien.gay@gm.univ-montp2.fr)

---

### Abstract :

Based on a High-Resolution 3D seismic block acquired in the Gulf of Lion in 2004-2005 we investigated fluid pipes and pockmarks on the top of the interfluvium between the Hérault canyon and the Bourcart canyon both created by turbidity currents and gravity flows from the shelf to the deep basin in the north-western Mediterranean Sea. Combining the geometry of the potential fluid pipes with the induced deformation of surrounding sediments leads then to the ability to differentiate between potential fluid sources (root vs source) and to better estimate the triggering mechanisms (allochthonous vs autochthonous cause). We linked together a set of derived attributes, such as Chaos and RMS amplitude, to a three dimensional description of pipes along which fluids may migrate. As previously shown in other basins, the induced deformation, creating cone in cone or V-shape structures, may develop in response to the fluid pipe propagation in unconsolidated sediments in the near surface. The level at the top of a cone structure is diachronous. It means that stratigraphic levels over this surface are deformed at the end of the migration. They collapse forming a depression called a pockmark. These pipes are the result of repeated cycles of fluid expulsion that might be correlated with rapid sea-level rise instead of sediment loading. The most recent event (MIS 2.2 stage) has led to the formation of a pockmark on the modern seafloor. It has been used as a reference for calculating the effect of a rapid sea-level rise on fluid expulsion. As all physical and geometrical parameters are constrained, we were able to define that a +34 m of sea level rise may account for triggering fluid expulsion from a very shallow silty-sandy layer at 9 m below seafloor since the last glacial stage. This value is consistent with a sea level rise of about 102 m during this period. This study shows that the episodic nature of fluid release resulted from hydromechanical processes during sea-level rise due to the interactivity between high pressure regimes and principal in situ stresses.

**Keywords :** pockmark, fluid overpressure, cycles, cone deformation

## 40 2. INTRODUCTION

41 Focused fluid migration in marine sediments is a widespread phenomenon which is  
42 increasingly gaining attention in the context of environmental discussions, even though it is still not  
43 well understood (Berndt, 2005). However, increased data coverage and the advent of new tools in  
44 oceanic exploration, such as backscatter imagery, multibeam swath bathymetry maps and 3D seismic  
45 data, can provide new evidence of relatively small-scale fluid seep structures on modern continental  
46 margins, and can help towards improving our understanding of the underlying processes. Fluid  
47 migration in sedimentary basins is an important process because 1) they accumulate into reservoirs  
48 that might be of economic interest; 2) the input of greenhouse gases into the ocean/atmosphere system  
49 may be an important component of the atmospheric carbon budget (Judd et al., 2002); 3) the fluid  
50 expulsion at the seafloor may play a role in potential instabilities on slopes (Prior and Coleman, 1984;  
51 Evans et al., 1996; Yun et al., 1999; Cochonat et al., 2002), representing a risk for human activities  
52 (Sultan et al., 2001; Elverhøi et al., 2002); and 4) fluid expulsion sites form the basis for a plethora of  
53 chemosynthetic benthic ecosystems that play an important role in the deep marine communities  
54 (Sibuet, 2003).

55 Since their initial identification on the Scotian Shelf by King and MacLean (King and  
56 MacLean, 1970), pockmarks have been reported repeatedly during offshore hydrocarbon exploration  
57 and scientific surveys in various depositional systems at water depths ranging from 30m to over 3000  
58 m (for a detailed review see Josenhans et al., 1978; Werner, 1978; Hovland, 1981; Whiticar and  
59 Werner, 1981; Hovland and Judd, 1988; Solheim and Elverhoi, 1993; Baraza and Ercilla, 1996; Rollet  
60 et al., 2006). They generally appear in unconsolidated, fine grained sediments as cone-shaped circular  
61 or elliptical depressions, ranging from a few meters to 800 m or more in diameter and from 1 m to 80  
62 m in depth, and they concentrate in fields extending over several square kilometers. In some cases,  
63 they have been identified along straight or circular lines correlated with glaciomarine tills (Josenhans  
64 et al., 1978; Whiticar and Werner, 1981; Kelley et al., 1994) suggesting a geological control on  
65 focused fluid flow (Eichhubl et al., 2000; Cifici et al., 2003; Gay et al., 2003). In particular, structural  
66 surfaces along bedrock (Shaw et al., 1997), salt diapirs (Taylor et al., 2000; Satyavani et al., 2005),  
67 faults and faulted anticlines (Boe et al., 1998; Soter, 1999; Vogt et al., 1999; Eichhubl et al., 2000;  
68 Dimitrov and Woodside, 2003) create pathways for fluid migration (Nakajima et al., in press). These  
69 observations suggest that discontinuities or unconformities are much more effective for fluid migration  
70 than a simple diffusive seepage through the sedimentary column (Abrams, 1992; Brown, 2000) and

71 are responsible for focused fluid flow, fluid escape at the seafloor and pockmark development  
72 (Abrams, 1992; Orange et al., 1999). The crater-like nature of pockmarks suggests an erosional power  
73 of fluid venting (Hovland and Judd, 1988), commonly related to an overpressured buried reservoir of  
74 biogenic gases, thermogenic gases, or oil, interstitial water, or a combination of the three. Time  
75 varying fluxes may be recorded into seafloor fluid seeps. An integrated study conducted on a giant  
76 pockmark of the Lower Congo Basin at 3200 m water depth has shown that the mineralogical,  
77 chemical, and biological facies are clearly related to upward fluid intensity (Gay et al., 2006c).

78 On the geophysical record, either 2D or 3D seismic data, pipes (or chimneys) are usually  
79 imaged as systematic disruptions and/or offset of the reflections within vertical zones, 50–1000 m  
80 wide and up to 1000 m high (Løseth et al., 2011). They are augmented by observations of amplitude  
81 enhancement or dimming. On seismic profiles, the pipe internal structure is characterized by  
82 reflections that are bent or offset upward (pull-up effect) or downward (pull-down effect) relative to  
83 the host stratigraphy by 20 to 150 ms TWT. Pipes are interpreted to represent a high-permeable  
84 vertical zone called a seal bypass system (Cartwright et al., 2007) caused by high fluid overpressure  
85 hydro-fracturing sediments of low permeability (Arntsen et al., 2007; Rodrigues et al., 2009). This  
86 geophysical characterization seems actually well constrained in space and time. However, neither the  
87 root of a pipe nor the triggering mechanisms are clearly defined. The interpretation of seismic data  
88 usually leads to a gap between the final result of fluid remobilization (i.e. fluid pipe and pockmarks  
89 recorded at the time of geophysical acquisition) and the physical causes that have triggered fluid  
90 migration in the past.

91 In the following sections, we will investigate fluid pipes and pockmarks located in the  
92 Gulf of Lion (Fig. 1). The final aim of this study is to link a set of derived attributes, such as Chaos  
93 and RMS amplitude, to a three dimensional description of pipes along which fluids may migrate and  
94 the induced deformation of surrounding host sediments. We will show that these pipes are the result of  
95 repeated cycles of fluid expulsion. Combining the geometry of the potential fluid pipes with cone-in-  
96 cone deformation structures using High-Resolution 3D seismic leads then to the ability to differentiate  
97 between potential fluid sources, root vs source (Gay et al., 2012) and to better estimate the triggering  
98 mechanisms (allochthonous vs autochthonous cause).

### 99 3. GEOLOGICAL SETTING

100 The HR 3D seismic area lies on the western flank of the Gulf of Lion (GoL) upper  
101 continental slope at 250-450 m water depth (Fig. 2). The GoL forms a crescent-shaped passive margin  
102 that is characterized by a 70 km wide continental shelf on the northwest part of the Mediterranean Sea.  
103 The Rhone River is the modern major source of sediment to the GoL shelf while other minor fluvial  
104 inputs also occur along the coastline (Pont et al., 2002). However, the buildup of the margin was  
105 strongly controlled by Quaternary glacial-interglacial sea-level variations (Rabineau et al., 2006;  
106 Frigola et al., 2012) and by significant subsidence at the shelf edge that has led to the deposition and

107 preservation of sedimentary bodies and to the incision of numerous canyons mainly oriented NW to  
108 SE and N to S (Berné et al., 2001; Baztan et al., 2005). The study area lies between two major  
109 canyons, the Bourcart Canyon and the Hérault Canyon (Fig. 2). The canyons display a marked axial  
110 incision that is interpreted as the imprint of erosive turbidity current initiated at the canyon head when  
111 it was connected to a river during the last sea-level low stand (Baztan et al., 2005). Actually,  
112 sediments are transported through the canyons by episodic dense shelf water formation and cascading  
113 events (DSWC) (Canals et al., 2006; Palanques et al., 2006; Pasqual et al., 2010; Sanchez-Vidal et al.,  
114 2008, 2012; Gaudin et al., 2006).

115 In situ testing carried out at 300 m long PRGL 1 (42°41'23.30"N, 3°50'15.50"E) and  
116 PRGL 2 (42°50'58.20"N, 3°39'30.85"E) boreholes (Fig. 2), have led to the identification of five  
117 main sequences (S1 to S5) stacked during the sea-level lowering phases of the last five glacial-  
118 interglacial 100-kyr cycles (Basetti et al., 2008). We used as a reference the commonly admitted D30-  
119 45-50-55-60-64-65-70 relative high sea-levels (Fig. 3), corresponding to each Dansgaard-Oeschger  
120 Greenland warm interstadial (Rabineau et al., 2006).

121 For geotechnical characterization, a continuous cone penetration test unified (CPTU) was  
122 performed at sites PRGL1 and PRGL2 (Lafuerza et al., 2008) but we used here only the PRGL1 as it  
123 was carried out within the area of HR 3D seismic acquisition. The test was made with a static  
124 penetrometer measuring cone resistance (kPa), sleeve friction (kPa) and pore pressure acting on the  
125 cone (kPa). Estimation of sediment types based on geotechnical properties was done using the method  
126 of soil classification established after Ramsey (2002). All geotechnical data were combined for soil  
127 characterization, considering that the pore pressure ( $u_2$ ) is mainly related to the permeability of  
128 sediments, whereas the resistance to cone penetration ( $q_t$ ) and the lateral friction ( $f_s$ ) can be directly  
129 correlated to a particular lithology (Fig. 3).

130 The lithologically homogeneous site PRGL1 is characterized by clays interbedded with  
131 silty-clays and locally sand to clayey sands (Lafuerza et al., 2008). Units I, III and IV are quite similar  
132 in terms of lateral friction ( $f_s$ ). Subunits IIb (from 33 to 36 mbsf), IIIc (70–72 mbsf), and IVd (120 –  
133 127 mbsf) comprise the reflectors corresponding to discontinuities D63, D60, and D50, which are  
134 found to represent intervals of variable thickness characterized by low friction measurements due to  
135 increased sand content. The lower unit V corresponds to S3. The rest of the boundaries between the  
136 CPTU-based subunits correspond to specific seismic reflectors defining different seismic facies:  
137 subunits IIa and IIIc correspond to low-amplitude hemistratified facies; IIIb, IVa, IVb, Va, and Vb to  
138 facies of intermediate amplitude; and IIIa, IIIb, and IVc to facies of higher relative amplitude  
139 (Lafuerza et al., 2008). Such changes in relative amplitude in the seismic record do correlate well with  
140 the CPTU-based geotechnical-stratigraphic divisions.

#### 141 4. DATA BASE AND PROCESSING

142 In 2004-2005 a High Resolution (HR 40-250 Hz) 3D seismic dataset was acquired in the  
143 Gulf of Lion over a 8.5x1.6 km area between the Bourcart canyon and the Hérault canyon ([Thomas et](#)  
144 [al., 2004](#); [Jouet, 2007](#)) (**Fig. 2**).

145 The HR3D seismic source consists of small volume air guns (mini-GI gun, 110 Hz  
146 dominant frequency) able to produce a repetitive signal. Two source arrays, 12.5 m apart, are fired  
147 alternately in order to have the cross-line sampling interval for a given number of streamers. Two  
148 streamers are deployed 25 m apart using two eight-meter long rigid bars fixed to the vessel's frame.  
149 Each streamer hosts 48 channels, with a 6.25 m group interval ([Thomas et al., 2012](#)). This seismic  
150 layout prevents spatial aliasing of dipping events up to 40° in the in-line direction and 20° in the cross-  
151 line direction. Positioning of sources and receivers is determined using the DGPS position and  
152 gyrocompass of the vessel, and magnetic compasses from 3 depth controllers along each streamer.  
153 Given the accuracy of these sensors and the short length of the streamers (400 meters), receiver  
154 positions are calculated within an absolute accuracy of 2 m at the head of the streamers, to 4 m at the  
155 tail. Source positions are measured to an absolute accuracy of 1 m. Positioning accuracy requirement  
156 to allow accurating wavefield reconstruction is  $l/4$  (where  $l$  is the dominant wavelength; [Gutowski et](#)  
157 [al. 2008](#)), thus 3.4 m considering the expected resolution given for the dominant wavelength (13.5 m  
158 @ 110 Hz). As the achieved positioning accuracy is between 2 and 4 m, the resulting resolution is  
159 slightly degraded.

160 Data editing and updating of the fold map are performed at the end of each line to assess  
161 the homogeneity of the data and to adjust the acquisition program to acquire additional in-fill lines to  
162 cover gaps in the fold map. Considering the relatively shallow water depth on the survey area,  
163 additional 2D HR seismic data recorded using longer source-receiver offset (490 m compared to the  
164 375 m maximum offset of the 3D layout) has allowed to constrain the velocity field within the upper  
165 sedimentary layers of interest ([Marsset et al., 2012](#)). A two-layer velocity model, 1515 m/s for the  
166 water column, and a constant gradient of 400 m/s increasing for the sediments was then applied to  
167 perform 3D stacking following by constant velocity two-pass Stolt time migration. The resulting  
168 seismic migrated volume should then reach a lateral resolution close to the 12.5 meters theoretical one.  
169 The vertical resolution is around 2.5 meters.

170 In the following study we derived seismic attributes from the amplitude of the HR 3D  
171 migrated dataset. However, free gas and/or carbonate cements have strong effects on the seismic  
172 signal and on the seismic amplitude as reflections can be respectively moved down or up. This is  
173 commonly attributed to a pull-down or a pull-up effect due to the migration during processing. So,  
174 seismic amplitude alone can be difficult to interpret in environments dominated by lateral and vertical  
175 fluid migrations through sediments. Due to the vertical pattern of seismic pipes (or chimneys) a typical  
176 horizon picking is not accurate to image them in a 3D domain. New tools in the academia and

177 petroleum exploration allow individualizing these chimneys from the 3D block (Gay et al, 2006; Gay  
178 et al., 2012):

179 The “RMS amplitude” ( $x_{rms}$ ) provides a scaled estimate of the trace envelope. It is  
180 computed in a sliding tapered window of  $N$  samples as the square root of the sum of all the trace  
181 values  $x_n$  squared:

$$x_{rms} = \sqrt{\frac{1}{N} \sum_{n=1}^N w_n x_n^2}$$

182 where  $w_n$  are the window values.

183 . The “Chaos attribute” is designed to measure the “lack of organization” in the dip and  
184 azimuth estimation method, based on the amplitude of reflectors and their continuity. Vertical and sub-  
185 vertical seismic pipes appear as homogeneous high-amplitude anomalies, ovoid in shape.

186 High RMS amplitude associated with a high chaotic signal pattern contained within  
187 seismic data can directly be related to the presence of fluids and or cements and thus can map  
188 hydrocarbon indications in the data and other geologic features which are isolated from background  
189 features by amplitude response (Gay et al., 2006, 2007). Alternatively, low RMS amplitude associated  
190 with a high chaotic signal pattern is rarely considered in seismic data. It can be used as a good  
191 indicator of the deformation of sediments induced by recent fluid motion through sediments, although  
192 coherency attribute alone gives only an indication of the deformation (Gay et al. 2012).

## 193 5. RESULTS

### 194 1. Morphology and structure of seafloor pockmarks

195 We identified more than 180 pockmarks in the study area with an average density of 13,2  
196 pockmarks per km<sup>2</sup> (Fig. 4). They range from 12,5 m (limit of seismic horizontal resolution) to 180 m  
197 in diameter, and from 4 to 15 ms TWT in depth with respect to the surrounding seabed. Most of them  
198 have a circular to sub-circular shape in plane view. The shaded relief map produced from the 3D  
199 seismic data shows that pockmarks are not randomly distributed on the seafloor (Fig. 4). They are  
200 mainly concentrated on the crest of a WNW-ESE striking anticline structure corresponding to the  
201 interfluvies between the Bourcart and the Herault canyons.

202 About 6 pockmarks, located in the North-East part of the 3D seismic area, are wider than  
203 100 meters. They are aligned parallel to the slope break of the Herault canyon (Fig. 4). The present  
204 Herault canyon is the last erosional episode of a series of glacial-interglacial 100-kyr cycles leading to  
205 incision-infill cycles. During these successive events, the canyon moved laterally creating a large  
206 valley. On the seismic section IL211, these pockmarks are aligned over a steep erosional surface of the  
207 paleo-canyon that incises into the upper slope (Fig. 5). As shown in the Lower Congo Basin (Gay et  
208 al.; 2007), fluids likely originate from deeper levels where they migrate laterally along dipping  
209 permeable stratigraphic units and more vertically along erosional unconformities or faults.



210 In the South-West part of the 3D seismic area, only a few small pockmarks, 10 to 15  
211 meters wide, have been identified (**Fig. 4**). They lie at the border of a terrace of the Bourcart canyon.  
212 They are probably related to a similar fluid migration pathway linked to a buried erosional surface. On  
213 the almost flat part of the terrace, no pockmarks have been detected. The infilling of the terrace is  
214 made of a succession of aggrading continuous and homogenous amplitude reflections interlayered  
215 with localized chaotic facies (**Fig. 5**). This seismic pattern is typically interpreted as Mass Transport  
216 Deposits (MTD's) and they probably come from instabilities on the flank of slope slidding towards the  
217 Bourcart canyon. Due to overconsolidation during the deposition process, MTD's are usually  
218 considered as an impermeable barrier (Gay et al., 2007b and references therein). Fluids migrate  
219 laterally towards the erosional surface where they are then driven upward and may accumulate and/or  
220 be expelled at the top of the anticline structure (Gay et al., 2007a).

221 As most of pockmarks are concentrated on the top of the anticline structure, we focused  
222 on this sub-area within the 3D seismic block. Pockmarks imprint the seafloor forming sub-circular  
223 depression, and they are often correlated with underlying depressions or amplitude anomalies.

## 224 **2. Seismic pipes**

225 Free gas can easily be interpreted from seismic records because even small amounts of  
226 gas within pore space significantly decrease the acoustic impedance of sediments and create anomalies  
227 such as acoustic turbidity, enhanced reflections (bright spots, flags) and acoustic blanking (wipe out)  
228 (Anderson and Hampton, 1980; Judd and Hovland, 1992; Schroot et al., 2005).

229 In most basins seismic profiles through pipes show two levels of acoustic anomalies,  
230 vertically elongated under the main depression (Gay et al., 2006). The deep anomaly is an inverted  
231 cone shape in cross section and it is marked by lower amplitude reflectors and acoustic turbidity. On  
232 both sides of this region the bright reflectors shift upward. This pull-up may be due to fluid movement  
233 (structural) or to velocity effects caused by hydrate/carbonate cementing within the overlying pipe  
234 corresponding to the shallow anomaly. The pipe is ovoid in shape with depressed high-amplitude  
235 reflectors considered as a reduction of the seismic velocities (pull-down effects), even if this could be  
236 real depressions due to fluid expulsion (ancient pockmarks?). Such acoustic anomalies are also called  
237 seismic chimneys and could be indicative of fluid flow from deeper levels (Hovland and Judd, 1988;  
238 Judd et al., 1992; Hempel et al., 1994; Heggland, 1997; Tingdahl et al., 2001; Ligtenberg, 2005).

239 On the seismic section IL211 a 250 ms TWT thick sub-vertical anomaly has been  
240 identified (**Fig. 5**). The pipe is the result of vertically stacked pull-down reflections, from 40 to 200 m  
241 in diameter. The main vertical axis of the pipe (i.e. the lowest part of each downbending reflection) is  
242 generally marked by higher amplitudes than the average amplitude along the reflections. The base of  
243 the pipe, or the root, seems to be at the D50 stratigraphic reflection. However, a single seismic section  
244 gives a partial view of the pipe. On a set of 9 seismic sections crosscutting the pipe (**Fig. 6**), the IL239  
245 clearly shows that the anomaly starts about 15 ms TWT above the D45 stratigraphic reflection. The  
246 base of the pipe is visible on IL239 to IL231 and stops at the D50 stratigraphic reflection. On IL227 to

247 IL219, there is no anomaly detected above or beneath the D50 stratigraphic reflection. On IL215 to  
 248 IL207, the pipe starts from the D50 stratigraphic reflection and propagates upward. High amplitude  
 249 anomalies within the pipe affect the D60 stratigraphic reflection on IL211 and 215 at about 560 ms  
 250 TWT. On IL215, from 475 to 525 ms TWT, downbending reflections are not continuous and they are  
 251 crosscut by a vertical anomaly characterized by polarity inversions at some points. This typical pattern  
 252 of a gas charged pipe propagates upward on IL 219 where it reaches the seafloor and connect to the  
 253 modern pockmark. The bottom of the main depression (i.e. the deepest point of the pockmark  
 254 compared to the regional seafloor) is located on IL219. However, high amplitude reflections forming a  
 255 vertically elongated anomaly are still visible on the south flank of the pockmark from IL227 to IL239.

256 This basic description of seismic anomalies clearly illustrates that a fluid pipe is not only  
 257 a vertical to sub-vertical conduit. Although seismic sections are commonly used for interpreting fluid  
 258 pipes, this method cannot be used to characterize all pipes present in a seismic block. A derived  
 259 attribute, the Chaos attribute, has been calculated and time slices are extracted every 50 ms from 400  
 260 ms to 750 ms TWT (**Fig. 7**). The Chaos attribute calculation is based on the amplitude variation and  
 261 the continuity of reflections. At 400 ms TWT, the dipping flanks of the major pockmarks, 40 to 200 m  
 262 wide, appear with a medium to high amplitude of Chaos. The bottom of the depression is low in  
 263 amplitude of Chaos, which is more consistent with surrounding regional sediments. The small  
 264 pockmarks, 20 to 40 m wide, are close to the detection limit and they appear as spots of medium to  
 265 high amplitude of Chaos. At 450 ms TWT, the time slice crosscut underlying pipes. They are  
 266 characterized by a ring of medium amplitude of Chaos that does correspond to the area where the  
 267 reflection starts to bend. The flanks are low in amplitude of Chaos and the axis of the pipe,  
 268 corresponding to the bottom of the depression, is medium to high in amplitude of Chaos. This pattern  
 269 would allow discrimination of pipes and ring and of pockmarks and paleo-pockmarks on a vertical  
 270 section. However, a paleo-pockmark and its associated underlying pipe can be re-used or reactivated  
 271 by later fluid migration and the geophysical signal might be modified, sometimes even shaded. This is  
 272 the case from 500 to 750 ms TWT where rings of medium to high amplitude of Chaos are vertically  
 273 correlated with spots or pipes of high amplitude of Chaos that appear over these features. This vertical  
 274 succession of amplitude anomalies shows that pockmarks can be reactivated, leading to the  
 275 development of a new pipe capped by a new pockmark until the fluid expulsion episode stops.

276 The large pockmark identified on seismic sections IL207 to IL239 (**see Fig. 5**) illustrates  
 277 the vertical succession of amplitude anomalies (**Fig. 7**). It is marked by flanks of high amplitude of  
 278 chaos down to 450 ms TWT. From 500 to 550 ms TWT the pipe is characterized by a ring of medium  
 279 amplitude of Chaos. At 600 ms TWT it transforms into a spot of high amplitude of Chaos. Below 650  
 280 ms TWT, no anomaly has been detected, which is consistent with the interpretation of a vertical  
 281 section showing that the base of the pockmark takes root right beneath the D45 stratigraphic level.

282 In such an approach, either characterizing a pipe on a vertical section or in time slices  
 283 using seismic amplitude and Chaos attribute, it is particularly difficult to define the root of each event



284 corresponding to the reactivation. For example, the root accounting for one event can be situated  
285 beneath the paleo-pockmark or within the pipe corresponding to the previous event.

### 286 **3. Constraining pipe geometry using horizontal dissection**

287 A new method for characterizing fluid pipes has been recently developed using sandbox  
288 models coupled to geophysical analysis (Mourgues et al., 2011, 2012; Gay et al., 2012). Based on the  
289 RMS amplitude, 7 levels of the fluid pipe have been identified from the D45 stratigraphic reflection to  
290 the seafloor (Fig. 8). About 200 time slices have been extracted. 19 time slices display the same  
291 pattern in which the base of a level is marked by a tiny spot of very low RMS amplitude. A ring of low  
292 RMS amplitude develops from the base and becomes greater to the top of the interval with an average  
293 diameter of 50 to 70 m for small depressions and an average diameter of 150-250 m for large  
294 depressions.

295 In a 3D view, the vertical succession of spots defines a stem and the flanks of the cone  
296 refer to as a corolla in a flower structure (Gay et al., 2012). It is interesting to note that the corolla on  
297 RMS amplitude is about 20% larger than the depression identified both on seismic amplitude and  
298 Chaos attribute.

## 299 **6. DISCUSSION**

300 In the Gulf of Lion (GoL) margin, western Mediterranean Sea, deltaic forced Regressive  
301 Progradational Units (RPU) stacked on the outer-shelf and upper slope during relative sea-level falls  
302 led some authors to describe this margin as a forced regressive system (Posamentier et al., 1992;  
303 Tesson et al., 1990, 2000). The significant subsidence rate of the margin, 250 m.Myr<sup>-1</sup> at the shelf edge  
304 (Rabineau, 2001), eased the preservation of RPU in the upper slope, as it was continuously  
305 submerged even during pronounced lowstands. These significant subsidence rate allowed preserving  
306 the majority of the regressive/transgressive depositional sequences across the outer shelf (former  
307 coastal deposits from old lowstand coast lines) and the upper slope accumulation where dating is  
308 easier, thus, resulting in an ideal area for the study of the late Quaternary sedimentary succession  
309 (Rabineau, 2001).

310 In this context, numerous fluid escape features, fluid pipes in the sedimentary column and  
311 related pockmarks at the seabed, provide evidence for a focused fluid flow system in the Gulf of Lion  
312 (Riboulot, 2011). The detailed observation of the pockmark geometry, obtained from High Resolution  
313 3D seismic volume, contributed to identify the evolution through time of the fluid pipes, which are  
314 interpreted as stacked pockmarks linked to the 100-kyr cyclicity within the hosting sedimentary  
315 sequences (lowstand periods). However, the mechanism by which focused fluids move up the  
316 sedimentary column to the surface is not well constrained. During burial, the sediment porosity  
317 decreases due to loading of overlying sediments. A set of processes, such as particle re-orientation and  
318 fluid expulsion, leads to the decrease of void spaces between particles (Maltman 1994; Vasseur et al.  
319 1995). Vertical migration of fluids through thick (up to 600 m), low permeability fine-grained

320 sediments cannot occur at a rate sufficient to explain the observed seafloor seeping structures in a  
321 context known to not be actually overpressured in shallow sediments (Lafuerza et al., 2008).

### 322 **Cone propagation and pockmark formation**

323

324 Several authors have used physical experiments to study the formation of piercement  
325 structures in various cases: kimberlite pipes (Walters et al., 2006), hydrothermal vents (Nermoen et al.,  
326 2010), mud volcanoes (Mazzini et al., 2009), or gas seeps (Varas et al., 2009, 2011). All these  
327 experiments involved non-cohesive materials such as glass microballs and sand which were fluidized  
328 by injecting locally a fluid (air or water). They obtained similar fluidization morphologies involving a  
329 large diverging cone-like structure of remobilized material just above the fluid injection. Nermoen et  
330 al. (2010) derived analytical solutions and concluded that fluidization occurs when the seepage forces  
331 integrated over the conical fluidized area balance the weight of the granular material (Mourgues and  
332 Cobbold, 2003). Furthermore, the role of fluid pressure in the re-opening of pre-existing fractures has  
333 long been emphasized (Grauls et al., 1994 and references therein). An increase in fluid pressure can lead  
334 to shearing (the minimum stress field is positive and the stress deviators are high) and the tensile  
335 failure (the minimum stress field is negative and the stress deviators are small). A context where the  
336 fluid pressure ( $P$ ) is almost equivalent to the minimum principal stress ( $\sigma_3$ ) will lead to the opening of  
337 fractures perpendicular to  $\sigma_3$ . So, such conditions favoring vertical fluid transfers are preferentially  
338 filled during periods of horizontal stress relaxation, once the minimum in situ stress field is less than  
339 the previously induced pressure regime ( $P > \sigma_3$ ). The consequence is a reduction of the stress deviator  
340 that will initiate a negative minimum effective stress field.

341 The pipe identified on the North-East corner of the 3D block in the Gulf of Lion may be  
342 characterized using RMS amplitude (Fig. 8). We identified 7 well individualized intervals of low RMS  
343 amplitudes. Each interval starts with a tiny point of low RMS amplitude which evolves upward as a  
344 ring and then suddenly disappears. In a 3D view, this corresponds to vertically stacked cone structures  
345 (Fig. 9). In general, the size of the ring is wider than the depression identified on seismic sections and  
346 on the Chaos attribute.

347 The seismic data suggest that the most accurate interpretation for a pipe boundary is at the  
348 transition from continuous layer reflections outside and the disturbed seismic pattern inside the pipe.  
349 The pipe-fill in the pipes may therefore be structureless as observed in outcrop (Løseth et al., 2011).  
350 This would imply that layered reflections inside the pipe are geophysical artifacts. However, laterally  
351 abrupt changes in impedance values may be due to enhanced density and/or velocity contrasts, which  
352 may be related to small-scale gas accumulations associated with fluid expulsion (Taylor et al., 2000).

353 As previously shown in the Gjallar Ridge (Gay et al., 2012), in the North-Sea (Mourgues  
354 et al., 2011) or in the Lower Congo Basin (Monnier et al., 2013), these cone structures identified using  
355 attributes derived from 3D seismic are due to the deformation of surrounding host sediments during  
356 upward fluid propagation. The flanks of a cone appear as discrete normal faults in sandbox models due

357 to the collapse after major fluid flow (Mourgues et al., 2012; Gay et al., 2012). However, the throw is  
358 smaller than can be resolved and the faults are not clearly seen in seismic profiles with the  
359 conventional amplitude attribute. The low RMS amplitude marking the flanks may be due to the shear  
360 effect along the fault plane, locally reorienting particles and dispersing energy of the seismic signal.

361 The top of a cone structure does correspond to the end of pipe propagation. Sandbox  
362 models have shown that the pipe propagation induces a seafloor uplift caused by inflation of fluid-  
363 charged sediments (Gay et al., 2012). The next step in the evolution of the structure would be a  
364 collapse creating sub-circular depressions, so-called pockmarks (Mourgues et al., 2011), i.e. structures  
365 defined by a basal unconformity is seismic stratigraphy (Andresen et al., 2011). In addition, buried  
366 depressions or pockmarks mark the end of the propagation process. The levels hosting pockmarks do  
367 not correspond to the time at which fluid migration started (Gay et al., 2012).

### 368 ***Triggering mechanisms***

369 Thanks to the combination of three CPTU measurements (cone resistance, lateral friction,  
370 pore pressure (Ramsey, 2002) it is possible to define the soil type based on a soil classification chart  
371 (Lafuerza et al., 2008). There is an apparent correlation between the soil type or the nature of  
372 sediments and fluid remobilization periods evidenced in the area. For example, the levels at which  
373 fluids are remobilized correspond to major lithological change, from sand or sandy-silty intervals to  
374 clayey to muddy intervals (Bassetti et al., 2007).

375 The conventional interpretation of seismic pipes leads to the conclusion that 7 repeated  
376 events of fluid expulsion occurred for the fluid pipe located at IL211. The strong deformation of  
377 surrounding sediments is interpreted as the result of fluid pipe propagation and in some extent, the  
378 basal unconformity outlining the depression marks the end of the fluid expulsion process. More  
379 precisely, the first continuous reflection sealing the depression and the faults signs the end the upward  
380 cone propagation and related fluid pipe activity. In consequence, the base of the V-shaped structure  
381 (the cone of deformation) represents the point of fluid injection (i.e. the top of reservoir) and clearly  
382 marks the base of chimneys or pipes. The top of the V-shaped structure marks the level attained by the  
383 fluid pipe. It doesn't mean that this surface is consistent with the seafloor. Sandbox models have  
384 shown that focused migration through vertical pipes may transform into a more distributed or diffuse  
385 migration a few meters beneath the seafloor (Gay et al., 2012). This is mainly due to less cohesive  
386 sediments and higher porosity and permeability in the sub-surface. It makes difficult to identify the  
387 level (i.e. the time) at which fluid migration was initiated, although our study shows that the base of  
388 the pipes can be interpreted using a set of attributes derived from the seismic data. Seismic  
389 interpretation of amplitude–time data may lead to misinterpretation of the base of pipes and thus leads  
390 to a wrong location of fluid pressure build-ups within the sedimentary basin.

391 In the absence of any calibration method, it is particularly difficult to estimate the  
392 sediment thickness above the point of injection that would help in determining the head pressure ( $\Delta h$ ).

393 However, the level at which fluids started to migrate upward is located between the top of the cone  
 394 structure and the base of the next overlying point of injection.

395 In the Gulf of Lion, core analysis in PRGL1 has shown that sediments are quite  
 396 homogeneous but they are mainly composed of fine sands – silty sands - interbedded with more shaly  
 397 intervals, playing the role of potential reservoirs and seal respectively. Fluids can migrate along both  
 398 erosional surfaces (see Fig. 5) delineating the Hérault canyon and the Bourcart canyon and they may  
 399 accumulate preferentially in the sandy-silty layers forming an anticline structure at the interfluvium.

400 However, due to the non-cohesive nature of sediments and high porosities and  
 401 permeabilities in the shallow sub-surface (Lafuerza et al., 2008), the dissipation of excess pore-  
 402 pressure is a very fast process. In order to create a focused fluid migration, an overpressure must be  
 403 generated at the point of injection:

404 **1) Effect of sediment loading:**

405 The vertical stress due to an additional load is:

$$406 \quad \sigma_v = \rho_{\text{sat}} \cdot d \quad (\text{Equation 1})$$

407 where  $\rho_{\text{sat}}$  is the bulk density (in  $\text{kN}\cdot\text{m}^{-3}$ ) and  $d$  is the thickness of the new deposit (in m). The average  
 408 bulk density in the core PRGL1 is about  $11,230 \text{ kN}\cdot\text{m}^{-3}$  with a vertical stress of about  $707 \text{ kN}\cdot\text{m}^{-2}$   
 409 (Lafuerza et al., 2008) Equation (1) gives a value of  $d$  equal or superior to about 63 m. The thickness  
 410 ( $d$ ) needed to create overpressure is about 63 m of sediments that must be deposited almost instantly  
 411 (at a geological time scale). In the area, the maximum thickness can be evaluated from event 7,  
 412 corresponding to the present day last event of fluid expulsion, and the effect of compaction is  
 413 minimized. The point of initiation, or the point of injection determined on RMS amplitude time-slices  
 414 (Fig. 8), is located at 434 ms TWT, corresponding to 9 m below seafloor. It means that the interval is  
 415 not thick enough to generate the required overpressure for focused pipe creation. Furthermore,  
 416 sedimentological core description does not evidence any catastrophic turbiditic events on the  
 417 interfluvium between the Hérault canyon and the Bourcart canyon and the average sedimentation rate is  
 418 only  $1 \text{ m}\cdot 10^3 \text{ yr}^{-1}$  (Bassetti et al., 2007; Dennielou et al., 2009).

419 The dissipation time of overpressured fluids ( $t_0$ ) depends on the hydraulic diffusivity  $D_z$   
 420 ( $1\cdot 10^{-8} \text{ m}^2\cdot\text{s}^{-1}$  in the study area, calculated from PRGL1), on the maximum vertical distance of  
 421 dissipation  $z$  (the dissipation can be performed upward or downward, so  $z = 9 / 2 = 4,5 \text{ m}$ ) and on a  
 422 time factor  $T_v$  (in %):

$$423 \quad t_0 = \frac{T_v \cdot (z)^2}{D_z} \quad (\text{Equation 2})$$

424  $T_v$  is related to the consolidation rate  $U$  (in %). The process of consolidation is directly  
 425 linked to the rate of excess pore pressure dissipation. The one dimensional consolidation theory is  
 426 governed by the following differential equation (Terzaghi, 1943):

$$427 \quad D_z \frac{\partial^2 u}{\partial z^2} = \frac{\partial u}{\partial t} \quad (\text{Equation 3})$$

428 where  $u$  is the pore water pressure,  $Dz$  is the hydraulic diffusivity,  $t$  is time and  $z$  denotes the position  
 429 where  $u$  is determined. The Terzaghi's consolidation equation can be solved using analytical or  
 430 numerical techniques. The solution obtained depends on the boundary conditions. For our case, with a  
 431 soil layer of height,  $2H$ , the boundary conditions are:

432 (a) complete drainage at top and bottom of the layer;  $u = 0$  at  $z = 0$  and  $z = 2H$ ;

433 (b) the initial excess pore water pressure  $\Delta u = u_i$  is equal to the applied stress increment  $\Delta \sigma$ .

434 The solution is obtained as a Fourier series, which can be expressed in the following form:

$$435 \quad U_z = 1 - \sum_{n=0}^{\infty} f_1\left(\frac{z}{H}\right) f_2(Tv) \quad (\text{Equation 4})$$

436 where  $U_z$  is the degree of consolidation at time  $t$ , at depth  $z$ , and  $Tv$  is a non-dimensional time factor.

437  $U_z$  and  $T$  are given by:

$$438 \quad Tv = Dz \frac{t}{H^2 ar} \quad (\text{Equation 5})$$

$$439 \quad U_z = -\frac{u}{u_i} \quad (\text{Equation 6})$$

440 where  $H_{dr}$  is the length of the longest drainage path. Based on the numerical solution of equation (4),  
 441 and in order to define the time factor  $T_v$  as a function of the degree of consolidation  $U_z$ , [Casagrande](#)  
 442 [\(1936\)](#) and [Taylor \(1948\)](#) determined a 'pre-calibrated' curve concerning the Time factor  $Tv$  which is  
 443 given by the following equations:

444  $U_z > 60\%$

$$445 \quad Tv = 1.78 - 0.933 \log(100 - U_z(\%)) \quad (\text{Equation 7})$$

$$446 \quad U_z > 60\% \quad Tv = \frac{\pi}{4} \left(\frac{U_z(\%)}{100}\right)^2 \quad (\text{Equation 8})$$

447 From equations (5), (7) and (8) and for a given hydraulic diffusivity  $Dz$  and a given  
 448 drainage path  $H_{dr}$ , it is possible to evaluate the time ( $t$ ) needed to get a specified degree of  
 449 consolidation  $U_z$ .

450 For a consolidation rate of 50%,  $Tv_{50\%}=0.197$  and Equation (2) gives a time dissipation of  
 451 about 4 years. For a consolidation rate of 99%,  $Tv_{99\%}=2$ , the time dissipation is about 37 years. It  
 452 means that for an average sedimentation rate of  $1 \text{ m} \cdot 10^3 \text{ yr}^{-1}$ , 9 m of sediments are deposited in 9000  
 453 years and the potential excess pore pressure is dissipated in 37 years for the best case of consolidation.  
 454 So, the effect of sediment loading alone cannot be taken into account for fluid expulsion in shallow  
 455 sediments of the Gulf of Lion.

## 456 **2) Effect of sea level variation**

457 In a sedimentary column, an elementary volume  $\Delta V$  is subjected to three forces:

458 (1) its own weight,  $F_g$ , due to gravity:

$$459 \quad F_g = \rho_{sat} \cdot \Delta V \quad (\text{Equation 9})$$

460 where  $\rho_{sat}$  is the specific gravity (in  $\text{kN} \cdot \text{m}^{-3}$ );

461 (2) forces of buoyancy,  $F_b$ , due to immersion in water:

$$462 \quad F_b = \rho_f \cdot \Delta V \quad (\text{Equation 10})$$

463 where  $\rho_f$  is the specific gravity of fluid (generally  $10 \text{ kN.m}^{-3}$ );

464 (3) seepage forces,  $F_s$ , due to fluid flow:

$$465 \quad F_s = i \cdot \rho_f \cdot \Delta V \quad (\text{Equation 11})$$

466 where  $\rho_f$  is the specific gravity of fluid and  $i$  is the hydraulic gradient, with  $i = -\text{Grad } h$ ,  
467 where  $h$  represents the head pressure.

468 Without any specific pathways where fluid may circulate and/or accumulate, pore fluids  
469 can escape up to the seafloor if sediments are fluidized: grains become suspended in fluid, which can  
470 migrate upward. Therefore, the balance between ascending forces ( $F_s$  and  $F_b$ ) and descending forces  
471 ( $F_g$ ) must be equal and the hydraulic gradient,  $i$ , must reach the critical gradient,  $i_c$ . For a vertical  
472 seepage,  $i_c$  is given by the following equations:

$$473 \quad \rho_{sat} \cdot dV = \rho_f \cdot dV + i_c \cdot \rho_f \cdot dv \quad (\text{Equation 12})$$

474 and

$$475 \quad \rho' = \rho_{sat} - \rho_f \quad (\text{Equation 13})$$

476 where  $\rho'$  corresponds to the submerged density. The equation (12) becomes:

$$477 \quad i_c = \frac{\rho'}{\rho_f} \quad (\text{Equation 14})$$

478 For fluid migration up to the seafloor, a vertical critical gradient must be taken into  
479 account from the point of initiation to the seafloor:

$$480 \quad i = \frac{\Delta H}{L} = i_c = \frac{\rho'}{\rho_f} \quad (\text{Equation 15})$$

481 where  $\Delta H$  is the variation of head pressures between the point of initiation and the  
482 seafloor and  $L$  represents the thickness between these two points.

483 For an average specific gravity,  $\rho_{sat}$ , of  $3,9 \text{ kN.m}^{-3}$  in the first 100 m of the sedimentary  
484 column calculated from PRGL1 site (Lafuerza et al. 2008), a specific gravity of seawater,  $\rho_f$ , of  $1,03$   
485  $\text{kN.m}^{-3}$ , and 9 m for  $L$  corresponding to the burial depth of the event 7 initiation point (9 m below  
486 seafloor), the variation of head pressure is 34,2 m, representing an excess pore pressure of 334 kPa  
487 (considering  $g$  equal to  $9,81 \text{ m.s}^{-1}$ ).

488 An excess pore pressure of 334 kPa can be created by a sea level rise, increasing pore  
489 water pressure at depth only in drained conditions. The needed sea level rise ( $H_1 - H_0$ ) for such an  
490 excess pore pressure able to create fluidization and expulsion can be calculated:

$$491 \quad \Delta P = (H_1 - H_0) \cdot \text{gradPs} \quad (\text{Equation 16})$$

492 Where  $\Delta P$  represents an excess pore pressure of 334 kPa at 9 m below seafloor,  $H_1$  is the  
493 actual bathymetry of 300 m,  $H_0$  is the initial bathymetry, and  $\text{gradPs}$  is about  $10,07 \text{ kPa.m}^{-1}$  in  
494 seawater. The calculated bathymetry,  $H_0$ , is about 266 m, giving a sea level rise of about +34 m.

495 The measurement of Relative Sea Level (RSL) can be done relative to present day Sea  
496 Level ( $t=0$ ). Paleobathymetry is usually estimated from cores with a description and evolution of  
497 sedimentary facies with microfossil assemblages (Ferland et al., 1995; Yokoyama et al., 2000;  
498 Hanebuth et al., 2000) and must be corrected from the subsidence effect. The most accurate study has



499 directly estimated the RSL in the western part of the Gulf of Lion from seismic data (Rabineau et al.,  
500 2006). They provided the position of the delta front at the last glacial maximum MIS2 giving an  
501 estimated value of  $102 \pm 6$  m at MIS 2.2 stage. This value is consistent with previous estimates in the  
502 region based on molluscs ages (Aloisi et al., 1975; Labeyrie et al., 1976; Aloisi et al., 1993) and also  
503 based on glacio-hydro isostatic modeling. More recent studies suggested a RSL of at least  $-115$  m but  
504 this value is not corrected from subsidence of the shelf (Jouet et al., 2006).

505 A sea level rise of about +34 m triggering fluid expulsion during event 7 is consistent  
506 with a global sea level rise of about 102 to 115 m since the last glacial maximum MIS 2.2 stage. A  
507 quick look at all other pipes present in 3D seismic area shows that the last event of fluid expulsion  
508 (event 7) is marked by cones of deformation accompanying the upward fluid pipe propagation. As the  
509 initiation point is situated at the same stratigraphic level, it means that most of the modern pockmarks  
510 were generated during the last sea level rise. Further investigations are required in order to check out  
511 whether the Gulf of Lion experienced a major fluid release since the last glacial stage as shown in  
512 other basins (Plaza-Faverola et al., 2011). For instance, in the Ceuta Drift and the Gulf of Cadiz, high  
513 resolution images have revealed that the pockmarks are connected to shallow subsurface reservoirs  
514 (Leon et al., 2010; Leon et al., 2014). In such environment, coarser-grained sediments can act as  
515 reservoirs for fluid accumulation and overlying fine-grained sediments may act as effective seals  
516 (Somoza et al., 2012; Leon et al., 2014). In this area, pockmarks are associated with the first  
517 subsurface erosion surface which is overlain by a transparent layer representing the final transgressive  
518 Holocene deposit (Leon et al., 2014). The decrease in hydrostatic pressure during the sea-level  
519 lowstand resulted in the expansion of sediment-trapped bubbles within the shallow subsurface  
520 reservoirs. At the same time, rhythmic tidal water level changes and large internal waves acted as  
521 "hydraulic pumps" of the shallow subsurface free gas accumulations (Leon et al., 2014). At the  
522 beginning of the transgressive period, seawater coming from the Atlantic Ocean started to overflow  
523 into the Mediterranean Sea creating internal waves (Leon et al., 2014). This event can be recorded at  
524 shallower depths ( $<100$  m) where the internal waves interacted with the sea bottom to form giant sand  
525 waves, like in the Gulf of Valencia (Albarracin et al., 2014). The propagation of internal waves  
526 alongshore may act together with the general sea-level rise at the beginning of the transgressive period  
527 as a hydraulic pump for fluids trapped at shallow depths, resulting in the formation of pockmarks  
528 (Leon et al., 2014). It means that, for each start of transgression, large amount of methane-rich fluids  
529 were possibly released into the ocean and atmosphere, possibly increasing the greenhouse effect  
530 (Dunkley Jones et al., 2010).

### 531 ***A model for cyclic fluid expulsions***

532 A recent geotechnical survey, conducted northwest and southeast of the study area  
533 (Sultan et al., 2007) has shown only one active gas emission within a pockmark. Based on in situ pore  
534 pressure measurements, they considered that the excess pore pressures and pockmark activities  
535 observed were most likely associated with the presence of free gas that partially saturated underlying

536 sedimentary layers. Furthermore, deep sea benthic analyses have shown that sediments within the  
537 active pockmark fields had lower meiofaunal abundance and biomass when compared with the  
538 surrounding sediments that were not influenced by the gas seepage (Zeppilli et al., 2012). All other  
539 investigated pockmarks in the area are inactive at the present day (Sultan et al., 2007; Zeppilli et al.,  
540 2012). This clearly indicates that 1) fluids are actively migrating from deeper levels. Given the  
541 geological context of the interfluvium, they are possibly driven through erosional surfaces or  
542 discontinuities; 2) fluids are accumulating in silt to sand-rich shallow buried levels leading to an actual  
543 increase in pore pressure; and 3) fluids are trapped under a low-permeability seal; and 4) fluids can  
544 escape at the seafloor in only a few places, the fluid escape is in a quiescence mode. This period is  
545 illustrated on Fig. 10 as stages A or E where there is a pressure build-up within a shallow buried silt-  
546 rich layer overlain by a mud-rich interval.

547

548 The pressure build-up is generated due to the fluid accumulation, leading to the  
549 development of a cone of deformation in overlying sediments and a bulge (or doming) at the seafloor  
550 (stage B, Fig. 10), as shown in other basins (Mourgues et al., 2012).

551 The possibility of dilatancy can be considered here due to erosion of the structure at the  
552 seafloor. The fluid pipe can vertically propagate along pre-formed cracks at stage B. Most of the fluids  
553 are released at this stage, leading to a collapse of the structure creating the seafloor depression (Gay et  
554 al., 2012; Dumke et al., 2014), or pockmark (stage C, Fig. 10). During stage B, the anticline structure  
555 developing between both turbiditic canyons is in a compressive regime bringing about a significant  
556 increase in fluid pressure although relaxation period alone will allow fluid to migrate upward at stage  
557 C. Then, during sea level highstand or continuing sea-level rise, the seafloor structures are smoothly  
558 draped by clayey hemipelagic sediments interlayered with thin beds of sand or silty sands (Bassetti et  
559 al., 2007) (Stage D, Fig. 10). This stage of draping is then accompanied or followed by a new period  
560 of fluid accumulation in more porous silty-sandy to sandy intervals, It can be called the recharge  
561 period (Stage E, Fig. 10). The next step is a new period of release unless the amplitude of sea level, or  
562 the depth of the reservoir, does not allow an excess pore pressure sufficient for triggering fluid  
563 expulsion.

## 564 7. Conclusion

565 3D seismic data provide new insights on the Gulf of Lion fluid migration history. It  
566 substantially improves the understanding of post-depositional processes that affect the sedimentary  
567 column in shallow subsurface. Analysis of such data makes it possible to understand the link between  
568 fluid pipes propagation and associated V-shaped structures. As previously shown in other basins, these  
569 cone structures may develop in response to the deformation of surrounding sediments during fluid  
570 migration in the near surface. They cannot be evidenced in a traditional way using seismic amplitude  
571 only and a set of derived attributes, such as RMS amplitude coupled to Chaos, must be calculated.

572 They allow the precise 3D mapping of the point of fluid injections in overlying sediments and the top  
573 of the cone structure marks the top of the focused migration. Based on these observations we focused  
574 on one example of fluid pipe characterized by repeated cycles of fluid expulsion. We have shown that  
575 these expulsion events might be correlated with sea level rise instead of sediment loading. The most  
576 recent event (event 7 corresponding to MIS 2.2 stage) has led to the formation of a pockmark on the  
577 modern seafloor. It has been used as a reference for calculating the effect of sea level rise on fluid  
578 expulsion. As all physical and geometrical parameters are constrained, we were able to define that a  
579 +34 m of sea level rise may account for triggering fluid expulsion since the last glacial stage. This  
580 value is consistent with a sea level rise of about 102 m during this period.

581 We propose a model that integrates with previous hypotheses. However, interpreting  
582 seismic facies alone doesn't provide the key for having the full picture of fluid migration processes in  
583 the shallow sub-surface. The assumption that the sea level rise, or the speed at which sea level is rising  
584 up, may be responsible for triggering fluid escape is highly relevant for predictive models describing  
585 the occurrence of pockmarks on slopes (implications for human activities such as cable, pipelines or  
586 platform anchors) and may account for large greenhouse gas release into the ocean and atmosphere  
587 (implication for climate change). The processes of fractures opening and fluid build-up in shallow  
588 reservoirs of lower pressure regimes preferentially occur during the relaxation phases of lateral  
589 tectonic stresses and as soon as the effective minimum stress become negative. Such conditions can be  
590 reached during sea-level rise in the Gulf of Lion.

## 591 **8. Acknowledgements**

592 We gratefully acknowledge the SHOM which co-acquired with IFREMER the HR 3D  
593 seismic data for this study. This project was supported by the Action-Marges funding, part of the  
594 French INSU program. We would like to thank miss Audrey Laplanche who was a master student  
595 involved in this project.

## 596 **9. List of Figures**

597 **Figure 1:** Location map of the study area in the Gulf of Lion, NW Mediterranean Sea. The 3D seismic  
598 dataset (white rectangle) is oriented NE-SW.

599 **Figure 2:** Shaded bathymetric map showing the Bourcart and Hérault canyons between 200 and 800  
600 m water depth (modified after Berné et al., 2004). The 3D seismic dataset is located on the interfluves  
601 between the canyons. The well PRGL 1 is located within the 3D seismic dataset allowing correlations.

602 **Figure 3:** Correlation between CPTU-based geotechnical stratigraphy and seismic reflection  
603 stratigraphy at PRGL1 site (modified from Lafuerza et al., 2008).

604 **Figure 4:** 3D shaded relief map extracted from the 3D seismic dataset. About 180 pockmarks have  
605 been identified on the seafloor. They are mostly concentrated on the top of the anticline structure  
606 corresponding to the interfluves between the Bourcart and the Hérault canyons.

607 **Figure 5:** Seismic profile IL 211 crossing the study area from NE to SW. This profile shows one of  
 608 the most prominent seismic anomaly beneath a seafloor pockmark located on the top of the interfluves  
 609 between the Bourcart and the Hérault canyons. Slopes on both sides of the interfluves are  
 610 characterized by erosional surfaces, onlap or drapping structures and high amplitude anomalies.

611 **Figure 6:** Zoomed in cross sections from IL 207 to IL 239 oriented NE-SW (See Fig. 4 and 5 for  
 612 location). This set of seismic profiles displays the 3D geometry of the anomaly beneath the pockmark.

613 **Figure 7:** Time slices of amplitude of Chaos from 400 ms TWT to 750 ms TWT (See Fig. 4 for  
 614 location). The pipes are represented by spots of high amplitude of chaos surrounded by rings of  
 615 medium amplitude of chaos.

616 **Figure 8:** RMS profile of IL 211 showing the vertical succession of anomalies from D45 stratigraphic  
 617 level to the seafloor (See Fig. 4, 5 and 7 for location). 7 intervals have been identified on RMS time  
 618 slices, starting at the base with a spot (the point of initiation) slightly evolving upward to a ring. This  
 619 structure defines a cone in 3D, or a V-shaped anomaly on 2D sections. They are associated with cones  
 620 of deformation that develop during a fluid pipe propagation (Mourgues et al., 2011, 2012; Gay et al.,  
 621 2012). The top of a cone marks the time at which the propagation started.

622 **Figure 9:** Correlation between the 7 cycles of pipe propagation and associated cone of deformation  
 623 and the sea level variation deduced from the  $\delta^{18}\text{O}$  curve. These expulsion events might be correlated  
 624 with sea level rise instead of sediment loading. The most recent event (event 7 corresponding to MIS  
 625 2.2 stage) has led to the formation of a seafloor pockmark.

626 **Figure 10:** Conceptual model for the development of a cyclic fluid expulsion: A) initiation during a  
 627 sea level rise, B) pipe propagation and associated cone of deformation, C) Seafloor collapse and major  
 628 fluid expulsion, D) end of expulsion and drapping, E) accumulation stage.

629

## 630 10. References

- 631 Abrams, M.A. 1992. Geophysical and geochemical evidence for subsurface hydrocarbon leakage in  
 632 the Bering Sea, Alaska. *Marine and Petroleum Geology Bulletin*, **9**, 208-221.
- 633 Albarracín, S., Alcántara-Carrió J., Montoya-Montes I., Fontán-Bouzas, A., Somoza, L. Amos, C.A.,  
 634 Rey, J. Relict wand waves in the continental shelf of the Gulf of Valencia (Western  
 635 Mediterranean). *Journal of Sea Research* 93, 33-46. Aloisi, J.C., Monaco, A., Thommeret, J. and  
 636 Thommeret, Y., 1975. Evolution paléogéographique du plateau continental languedocien dans  
 637 le cadre du golfe du Lion; Analyse comparée des données sismiques, sédimentologiques et  
 638 radiométriques concernant le Quaternaire récent. *Rev. Géogr. Phys. Géol. Dyn.*, 17(1): 13–22.
- 639 Aloisi, J.C., 1993. Sea Level Variations on the French Mediterranean Margin during the Holocene.  
 640 *Paleoclimate Research; Paläklimateforschung n°spec: 25.*
- 641 Anderson, A. and Hampton, L.D., 1980. Acoustics of gas-bearing sediments .2. Measurements and  
 642 models. *Journal of Acoustical Society of America*, 67: 1890-1903.
- 643 Andresen, K.J. and Huuse, M., 2011. "Bulls-eye" pockmarks and polygonal faulting in the Lower  
 644 Congo Basin: relative timing and implications for fluid expulsion during shallow burial. *Marine  
 645 Geology*, 279(1-4): 111-127.

- 646 Arntsen, B., Wensaas, L., Løseth, H. and Hermanrud, C., 2007. Seismic modelling of gas chimneys.  
647 *Geophysics*, 72: 251-259.
- 648 Baraza, J. and Ercilla, G., 1996. Gas-charged sediments and large pockmark-like features on the Gulf  
649 of Cadiz slope (SW Spain). *Marine and Petroleum Geology*, 13(2): 253-261.
- 650 Baztan, J., Berné, S., et al., 2005. Axial incision: The key to understand submarine canyon  
651 evolution (in the western Gulf of Lion). *Marine and Petroleum Geology*, 22(6-7): 805-826.
- 652 Bassetti, M.A. et al., 2008. The 100-ka and rapid sea level changes recorded by prograding shelf sand  
653 bodies in the Gulf of Lions (western Mediterranean Sea). *Geochemistry Geophysics  
654 Geosystems*, 9(11): doi:10.1029/2007GC001854.
- 655 Berndt, C. 2005. Focused fluid flow on continental margins. *Philosophical Transactions of the Royal  
656 Society Series A*, **363**, 2855-2871.
- 657 Berné, S., Carré, D., Loubrieu, B., Mazé, J.-P. and Normand, A., 2001. Carte morphobathymétrique du  
658 Golfe du Lion à l'échelle 1/100 000ème. IFREMER et Région Languedoc Roussillon, Brest.
- 659 Berné, S., M. Rabineau, J.A. Flores, and F.J. Sierro. 2004. The impact of quaternary global changes on  
660 strata formation: Exploration of the shelf edge in the northwest Mediterranean Sea.  
661 *Oceanography* 17(4):92–103, <http://dx.doi.org/10.5670/oceanog.2004.07>.
- 662 Boe, R., Rise, L. and Ottesen, D., 1998. Elongate depressions on the southern slope of the Norwegian  
663 trench(Skagerrak) : morphology and evolution. *Marine Geology*, 146: 191-203.
- 664 Brown, A. 2000. Evaluation of possible gas microseepage mechanisms. *AAPG Bulletin*, **84**, 1775-  
665 1789.
- 666 Canals, M. et al., 2006. Flushing submarine canyons. *Nature*, 444: 354–357.
- 667 Cartwright, J., Huuse, M. and Aplin, A.C., 2007. Seal bypass system. *AAPG bulletin*, 91(8): 1141-  
668 1166.
- 669 Casagrande, A., 1936. Characteristics of cohesionless soils affecting the stability of slopes and earth  
670 fills. *Journal of Boston Soc. Civil Engrs.*, Vol. 23: p. 13-32.
- 671 Cifci, G., Dondurur, D. and Ergun, M., 2003. Deep and shallow structures of large pockmarks in the  
672 Turkish shelf, Eastern Black Sea. *Geo-Marine Letters*, 23: 311-322.
- 673 Cochonat, P. et al., 2002. Slope instabilities and gravity processes in fluid migration and tectonically  
674 active environment in the eastern Nankai accretionary wedge (KAIKO-Tokai'96 cruise). *Marine  
675 Geology*, 187: 193-202.
- 676 Dennielou, B. et al., 2009. Post-glacial persistence of turbiditic activity within the Rhone deep-sea  
677 turbidite system (Gulf of Lions, Western Mediterranean): Linking the outer shelf and the basin  
678 sedimentary records *Marine Geology*, 257(1-4): 65-86.
- 679 Dimitrov, L. and Woodside, J., 2003. Deep sea pockmarks environments in the eastern Mediterranean.  
680 *Marine Geology*, 195: 263-276.
- 681 Dumke, I., Berndt, C., Crutchley, G.J., Krause, S., Liebetrau, V., Gay, A., Couillard, M., 2014. Seal  
682 bypass at the Giant Gjallar Vent (Norwegian Sea): Indications for a new phase of fluid venting  
683 at a 56-Ma-old fluid migration system. *Marine Geology*, 351: 38-52.
- 684 Dunkley Jones, T. et al., 2010. A Palaeogene perspective on climate sensitivity and methane hydrate  
685 instability. *Philosophical Transactions of the Royal Society a-Mathematical Physical and  
686 Engineering Sciences*, 368(1919): 2395-2415.
- 687 Eichhubl, P., Greene, H.G., Naehr, T. and Maher, N., 2000. Structural control of fluid flow: offshore  
688 fluid seepage in the Santa Barbara Basin, California. *Journal of Geochemical Exploration*,  
689 69/70: 545-549.
- 690 Elverhoi, A., De Blasio, F.V., Butt, F.A., Issler, D., Harbitz, C.B., Engvik, L., Solheim, A. & Marr, J.,  
691 2002. Submarine mass-wasting on glacially influenced continental slopes - processes and  
692 dynamics. In: Dowdeswell, J.A. & O'Cofaigh, C. (eds), *Glacier-influenced Sedimentation on  
693 high Latitude Continental Margins*. Geological Society, London, Special Publication, **203**, 73-  
694 87.

- 695 Evans, D., King, E.L., Kenyon, N.H., Brett, C. & Wallis, D. 1996. Evidence for long-term instability  
696 in the Storegga Slide region off western Norway. *Marine Geology*, **130**, 281-292.
- 697 Ferland, M., Roy, P. and Murray-Wallace, C., 1995. Glacial lowstand deposits on the outer continental  
698 shelf of Southeastern Australia. *Quaternary Research*, 44: 294–299.
- 699 Frigola, J. et al., 2012. A 500 kyr record of global sea-level oscillations in the Gulf of Lion,  
700 Mediterranean Sea: new insights into MIS 3 sea-level variability. *Climate Past*, 8: 1067–1077.
- 701 Gaudin, M. et al., 2006. Massive sand beds attributed to deposition by dense water cascades in the  
702 Bourcart canyon head, Gulf of Lions (northwestern Mediterranean Sea). *Marine Geology*, 234:  
703 111–128.
- 704 Gay, A. et al., 2003. Sinuous pockmark belt as indicator of a shallow buried turbiditic channel on the  
705 lower slope of the Congo Basin, West African Margin. In: P. Van Rensbergen, R.R. Hillis, A.J.  
706 Maltman and C.K. Morley (Editors), *Subsurface Sediment Mobilization*. Special Publications.  
707 Geological Society of London, pp. 173-189.
- 708 Gay, A. et al., 2006. Seafloor facies related to upward methane flux within a Giant Pockmark of the  
709 Lower Congo Basin. *Marine Geology*, 226(1-2): 81-95.
- 710 Gay, A. et al., 2006. Isolated seafloor pockmarks linked to BSRs, fluid chimneys, polygonal faults and  
711 stacked Oligocene-Miocene turbiditic palaeochannels in the Lower Congo Basin. *Marine  
712 Geology*, 226: 25-40.
- 713 Gay, A. et al., 2006. Evidences of early to late fluid migration from an upper Miocene turbiditic  
714 channel revealed by 3D seismic coupled to geochemical sampling within seafloor pockmarks,  
715 Lower Congo Basin. *Marine and Petroleum Geology*, 23: 387-399.
- 716 Gay, A., Lopez, M., Berndt, C. and Séranne, M., 2007a. Geological controls on focused fluid flow  
717 associated with seafloor seeps in the Lower Congo Basin. *Marine Geology*, 244: 68-92.
- 718 Gay, A. & C. Berndt, 2007b. Cessation/reactivation of polygonal faulting and effect on fluid flow in  
719 the Voring Basin, Norwegian Margin. *Journal of the Geological Society of London*. Vol. 164,  
720 129-141.
- 721 Gay, A. et al., 2012. Anatomy of a fluid pipe in the Norway Basin: Initiation, propagation and 3D  
722 shape. *Marine Geology*, 332: 75-88.
- 723 Grauls, D. and Baleix, J.M., 1994. Role of overpressures and in situ stresses in fault controlled  
724 hydrocarbon migration: a case study. *Marine and Petroleum Geology*, 11(6): 734-742.
- 725 Gutowski, M. et al., 2008. Three-dimensional high-resolution acoustic imaging of the sub-seabed.  
726 *Applied Acoustics*, 69: 412-421.
- 727 Hanebuth, T., Statterger, K. and Grootes, P.M., 2000. Rapid flooding of the Sunda Shelf: a Late-  
728 Glacial sea-level record. *Science*, 288: 1033–1035.
- 729
- 730 Heggland, R., 1997. Detection of gas migration from a deep source by the use of exploration 3D  
731 seismic data. *Marine Geology*, 13: 41-47.
- 732 Hempel, P., Spiess, V. & Schreiber, R. 1994. Expulsion of shallow gas in the Skagerrak- Evidence  
733 from subbottom profiling, seismic, hydroacoustical and geochemical data. *Estuarine, Coastal  
734 and Shelf Science*, **38**, 583-601.
- 735 Hovland, M., 1981. Characteristics of pockmarks in the Norwegian trench. *Marine Geology*, 39: 103-  
736 117.
- 737 Hovland, M. and Judd, J., 1988. Seabed pockmarks and seepages. *Impact on Geology, Biology and  
738 Marine Environment*. Graham and Trotman, London, 293 pp.
- 739 Josenhans, H.W., King, L.H. and Fader, G.B., 1978. A side-scan sonar mosaic of pockmarks on the  
740 Scotian shelf. *Canadian Journal of Earth Sciences*, 15: 831-840.
- 741 Jouet, G. et al., 2006. Shoreface migrations at the shelf edge and sea-level changes around the Last  
742 Glacial Maximum (Gulf of Lions, NW Mediterranean). *Marine Geology*, 234: 21–42.
- 743 Jouet, G. 2007. Enregistrements stratigraphiques des cycles climatiques et glacio-eustatiques du  
744 Quaternaire terminal-Modélisations de la marge continentale du Golfe du Lion, PhD Thesis,



- 745 Laboratoire Environnements Sédimentaires, Géosciences Marines. Ifremer, Brest, France, 443  
746 pp.
- 747 Judd, A.G., Hovland, M., Dimitrov, L.I., Garcia Gil, S. and Jukes, V., 2002. The geological methane  
748 budget at continental margins and its influence on climate change. *Geofluids*, 2: 109-126. Judd,  
749 A.G. and Hovland, M., 1992. The evidence of shallow gas in marine sediments. *Continental  
750 Shelf Research*, Vol. 12(No. 10): p. 1081-1095.
- 751 Judd, A., Long, D. and Sankey, M., 1992. Pockmark formation and activity, UK block 15/25, North  
752 Sea. *Bulletin of the Geological Society of Denmark*, 41: 34-49.
- 753 Kelley, J.T., Dickson, S.M., Belknap, D.F., Barnhardt, W.A. and Henderson, M., 1994. Giant sea-bed  
754 pockmarks: evidence for gas escape from Belfast Bay, Maine. *Geology*, 22: 59-62.
- 755 King, L.H. and MacLean, B., 1970. Pockmarks on the Scotian shelf. *Geological Society of America  
756 Bulletin*, Vol. 81: p. 3141-3148.
- 757 Labeyrie, J., Lalou, C., Monaco, A. and Thommeret, J., 1976. Chronologie des niveaux eustatiques sur  
758 la côte du Roussillon de-33000 ans B.P. à nos jours. *Comptes Rendus de l'Académie des  
759 Sciences de Paris*, 282: 349–352.
- 760 Lafuerza, S. et al., 2008. Subseafloor stratigraphic profiling and soil classification from piezocone  
761 tests: A case study in the Gulf of Lion (NW Mediterranean Sea). *Geochemistry Geophysics  
762 Geosystems*, 9(12): Q12028.
- 763 León, R., Somoza, L., Medialdea, T., Gonzalez, FJ, Gimenez-Moreno, CJ, Perez-Lopez, R. (2014).  
764 Pockmarks on either side of the Strait of Gibraltar: formation from overpressured shallow  
765 contourite gas reservoirs and internal wave action during the last glacial sea-level lowstand?.  
766 *Geo-Marine Letters* Volume: 34 2-3: 131-151.
- 767 León R, Somoza L, Medialdea T, Hernández-Molina FJ, Vázquez JT, Díaz-del-Río V, González FJ  
768 (2010) Pockmarks, collapses and blind valleys in the Gulf of Cádiz. *Geo-Marine Letters*  
769 30(3/4):231–247.
- 770 Ligtenberg, H., 2005. Detection of fluid migration pathways in seismic data: implications for fault seal  
771 analysis. *Basin Research*, 17: 141-153.
- 772 Løseth, H. et al., 2011. 1000 m long gas blow-out pipes. *Marine and Petroleum Geology*, 28: 1047-  
773 1060.
- 774 Maltman, A., 1994. *The Geological Deformation of Sediments*, Chapman & Hall, London, 362 p.
- 775 Marsset B., Thomas, Y., Sultan, N., Gaillot, A., Stephan, Y. (2012). A multi-disciplinary approach to  
776 marine shallow geohazard assessment. *Near Surface Geophysics*, 10(4), 279-288.  
777 <http://dx.doi.org/10.3997/1873-0604.2012012>
- 778 Mazzini, A. et al., 2009. Strike-slip faulting as a trigger mechanism for overpressure release through  
779 piercement structures. Implications for the Lusi mud volcano, Indonesia. *Marine and Petroleum  
780 Geology*, 26(9): 1751–1765.
- 781 Monnier, D., Imbert, P., Gay, A., Lopez, M. and Mourgues, R., (2012). Pliocene sand injectites from a  
782 submarine lobe fringe during hydrocarbon migration (and sal diapirism): a seismic example  
783 from the Lower Congo Basin. *Geofluids*.
- 784 Mourgues, R. and Cobbold, P.R., 2003. Some tectonic consequences of fluid overpressures and  
785 seepage forces as demonstrated by sandbox modelling. *Tectonophysics*, 376: 75-97.
- 786 Mourgues, R., Bureau, D., Bodet, L., Gay, A. and Gressier, J., 2012. Formation of conical fractures in  
787 sedimentary basins: Experiments involving pore fluids and implications for sandstone intrusion  
788 mechanisms. *Earth and Planetary Science Letters*, 313: 67-78.
- 789 Mourgues, R., Gressier, J.B., Bodet, L., Bureau, D. and Gay, A., 2011. “Basin scale” versus  
790 “localized” pore pressure/stress coupling e Implications for trap integrity evaluation. *Marine and  
791 Petroleum Geology*, 28(5): 1111-1121.
- 792 Nakajima, T. et al., in press. Formation of pockmarks and submarine canyons associated  
793 with dissociation of gas hydrates on the Joetsu Knoll, eastern margin of the Sea of  
794 Japan. *Journal of Asian Earth Sciences*.

- 795 Nermoen, A. et al., 2010. Experimental and analytic modeling of piercement structures. *Journal of*  
796 *Geophysical Research-Solid Earth*, 115(B10202).
- 797 Orange, D.L., Greene, H.G., Reed, D., Martin, J.B., McHugh, C.M., Ryan, W.B.F., Maher, N., Stakes,  
798 D. & Barry, J. 1999. Widespread fluid expulsion on a translational continental margin: Mud  
799 volcanoes, fault zones, headless canyons, and organic-rich substrate in Monterey Bay,  
800 California. *Geological Society of America Bulletin*, **111**, 992-1009.
- 801 Palanques, A. et al., 2006. Suspended sediment fluxes and transport processes in the Gulf of Lions  
802 submarine canyons. The role of storms and dense water cascading. *Marine Geology*, 234: 43–  
803 61.
- 804 Pasqual, C. et al., 2010. Flux and composition of settling particles across the continental margin of the  
805 Gulf of Lion: the role of dense shelf water cascading. *Biogeosciences*, 7: 217–231.
- 806 Plaza-Faverola, A., Bunz, S. and Mienert, J., 2011. Repeated fluid expulsion through sub-seabed  
807 chimneys offshore Norway in response to glacial cycles. *Earth and Planetary Science Letters*,  
808 305(3-4): 297-308.
- 809 Pont, D., Simonnet, J.P. and Walter, A.V., 2002. Medium-term Changes in Suspended Sediment  
810 Delivery to the Ocean: Consequences of Catchment Heterogeneity and River Management  
811 (Rhône River, France). *Estuarine, Coastal and Shelf Science*, 54: 1–18.
- 812 Posamentier, H.W., Allen, G.P., James, D.P. and Tesson, M., 1992. Forced regressions in a sequence  
813 stratigraphic framework: concepts, examples, and exploration significance. *AAPG bulletin*, 76:  
814 1687–1709.
- 815 Prior, D.B. and Coleman, J.B., 1984. Submarine slope instability. In: D. Brunsten and D.B. Prior  
816 (Editors), *Slope Instability*. Wiley, New York, pp. 419-455.
- 817 Rabineau, M., 2001. Un modèle géométrique et stratigraphique des séquences de dépôts quaternaires  
818 de la plate-forme du Golfe du Lion: enregistrement des cycles glacioeustatiques de 100 000  
819 ans., Université de Rennes, Rennes, 392 pp.
- 820 Rabineau, M. et al., 2006. Paleo sea levels reconsidered from direct observation of paleoshoreline  
821 position during Glacial Maxima (for the last 500,000 yr). *Earth and Planetary Science Letters*,  
822 252: 119–137.
- 823 Ramsey, N., 2002. A calibrated model for the interpretation of cone penetration tests (CPTs) in North  
824 Sea quaternary soils. In: M.e.a. Cook (Editor), *Offshore Site Investigation and Geotechnics:*  
825 *Diversity and Sustainability*. Society for Underwater Technology, London, pp. 341–356.
- 826 Riboulot, V., 2011. Facteurs de contrôle du fonctionnement des pockmarks durant les derniers cycles  
827 climatiques (Partie orientale du delta sous-marin du Niger et Golfe du Lion), Université de  
828 Perpignan Via Domitia, Perpignan, France, 243 pp.
- 829 Rodrigues, N., Cobbold, P.R. and Løseth, H., 2009. Physical modelling of sand injectites.  
830 *Tectonophysics*, 474: 610-632.
- 831 Rollet, N. et al., 2006. Characterisation and correlation of active hydrocarbon seepage using  
832 geophysical data sets: An example from the tropical, carbonate Yampi Shelf, Northwest  
833 Australia. *Marine and Petroleum Geology*, 23(2): 145-164.
- 834 Sanchez-Vidal, A. et al., 2008. Impact of dense shelf water cascading on the transfer of organic matter  
835 to the deep western Mediterranean basin. *Geophysical Research Letters*, 35: L05605.
- 836 Satyavani, N., Thakur, N.K., Aravind Kumar, N. and Reddi, S.I., 2005. Migration of methane at the  
837 diapiric structure of the western continental margin of India. *Marine Geology*, 219: 19-25.
- 838 Schroot, B.M., Klaver, G.T. and Schüttenhelm, R.T.E., 2005. Surface and subsurface expressions of  
839 gas seepage to the seabed - examples from the Southern North Sea. *Marine and Petroleum*  
840 *Geology*, 22: 499-515.
- 841 Shaw, J., Courtney, R.C. and Currie, J.R., 1997. Marine geology of St. George's Bay, Newfoundland,  
842 as interpreted from multibeam bathymetry and back-scatter data. *Geo-Marine Letters*, 17: 188-  
843 194.

- 844 Sibuet, M., 2003. Cold seep communities on continental margins; structure and quantitative  
845 distribution relative to geological and fluid venting patterns. In: G. Wefer et al. (Editors), Ocean  
846 margin systems. Springer-Verlag, Bremen, pp. 235-251.
- 847 Solheim, A. and Elverhoi, A., 1993. Gas-related sea floor craters in the Barents Sea. *Geo-Marine*  
848 *Letters*, 13: 235-243.
- 849 Somoza, L., Medialdea T., R. León, G. Ercilla, J. T. Vázquez, M. Farran, J. Hernández-Molina, J.  
850 González, C. Juan, M. C. Fernández-Puga. (2012) Structure of mud volcano systems and  
851 pockmarks in the region of the Ceuta Contourite Depositional System (Western Alborán Sea).  
852 *Marine Geology* 332–334: 4–26
- 853 Soter, S., 1999. Macroscopic seismic anomalies and submarine pockmarks in the Corinth-Patras rift,  
854 Greece. *Tectonophysics*, 308: 275-290.
- 855 Sultan, N., Cochonat, P., Bourillet, J.-F. and Cayocca, F., 2001. Evaluation of the risk of marine slope  
856 instability: a pseudo-3D approach for application to large areas. *Marine Georesources and*  
857 *Geotechnology*, 19: 107-133.
- 858 Sultan, N., Gaudin, M., Berne, S., Canals, M., Urgeles, R. & Lafuerza, S. (2007) Analysis of slope  
859 failures in submarine canyon heads: an example from the Gulf of Lions. *Journal of Geophysical*  
860 *Research*, 112, F01009.
- 861 Taylor, D.W., 1948. *Fundamentals of soil mechanics*. John Wiley, New York.
- 862 Taylor, M.H., Dillon, W.P. and Pecher, I.A., 2000. Trapping and migration of methane associated with  
863 the gas hydrate stability zone at the Blake Ridge Diapir: new insights from seismic data. *Marine*  
864 *Geology*, 164: 79-89.
- 865 Terzaghi, K., 1943. *Theoretical soil mechanics*. John Wiley, New York.
- 866 Tesson, M., Gensous, B., Allen, G.P. and Ravenne, C., 1990. Late Quaternary deltaic lowstand  
867 wedges on the Rhône continental shelf, France. *Marine Geology*, 91: 325–332.
- 868 Tesson, M., Posamentier, H.W. and Gensous, B., 2000. Stratigraphic organization of late pleistocene  
869 deposits of the western part of the Golfe du Lion shelf (Languedoc shelf), Western  
870 Mediterranean Sea, using high-resolution seismic and core data. *AAPG bulletin*, 84: 119–150.
- 871 Thomas Y., Marsset B., Didailier S., Regnault J.P., Le Conte S., Le Roux D., Farcy P., Magueur M.,  
872 Violette P., Herveou J., Guedes J.C., Jegot B., Gascon G., Prud'homme C., Nouzé H., Thereau  
873 E., Contrucci I. and Foucher J.P. 2004. High Resolution marine 3D seismic: A new surveying  
874 tool for the Scientific Community. *Comptes Rendus Géoscience* **336**, 579–585.
- 875 Thomas, Y. et al., 2012. Contribution of high-resolution 3D seismic near-seafloor imaging to  
876 reservoir-scale studies: application to the active North Anatolian Fault, Sea of Marmara. *Near*  
877 *Surface Geophysics*, 10: 291-301.
- 878 Tingdahl, K.M., Bril, A.H. & de Groot, P.F. 2001. Improving seismic chimney detection using  
879 directional attributes. *Journal of Petroleum Science and Engineering*, **29**, 205-211.
- 880 Varas, G., Vidal, V. and Geminard, J.J., 2009. Dynamics of crater formations in immersed granular  
881 materials. *Physical Review E*, 79(2): 021301(7).
- 882 Varas, G., Vidal, V. and Geminard, J.J., 2011. Venting dynamics of an immersed granular layer.  
883 *Physical Review E*, 83(1): 011302(6).
- 884 Vasseur, G., Djeran-Maigre, I., Grunberger, D., Rousset, G., Tessier, D. & Velde, B. 1995. Evolution  
885 of structural and physical parameters of clays during experimental compaction. *Marine and*  
886 *Petroleum Geology*, **12**, 941-954.
- 887 Vogt, P.R., Gardner, J. and Krane, K., 1999. The Norwegian-Barents-Svalbard (NBS) continental  
888 margin: Introducing a natural laboratory of mass wasting, hydrates, and ascent of sediment, pore  
889 water, and methane. *Geo-Marine Letters*, 19: 2-21.
- 890 Walters, A.L. et al., 2006. The role of fluidisation in the formation of volcanoclastic kimberlite: Grain  
891 size observations and experimental investigation. *J. Volcanol. Geotherm. Res.*, 155: 119–137.
- 892 Werner, F., 1978. Depressions in mud sediments (Eckernfoerde Bay, Baltic Sea) related to sub-bottom  
893 and currents. *Meyniana*, 30: 99-104.

894 Whiticar, M.J. and Werner, F., 1981. Pockmarks : Submarine vents of natural gas or freshwater seeps  
895 ? Geo-Marine Letters, 1: 193-199.

896 Yokoyama, Y., Lambeck, K., Johnston, P. and Fifield, L.K., 2000. Timing of the Last Glacial  
897 Maximum from observed sea-level minima. Nature, 406: 713–716.

898

899 Yun, J.W., Orange, D.L. and Field, M.E., 1999. Subsurface gas offshore of northern California and its  
900 link to submarine geomorphology. Marine Geology, Vol. 154: p. 357-368.

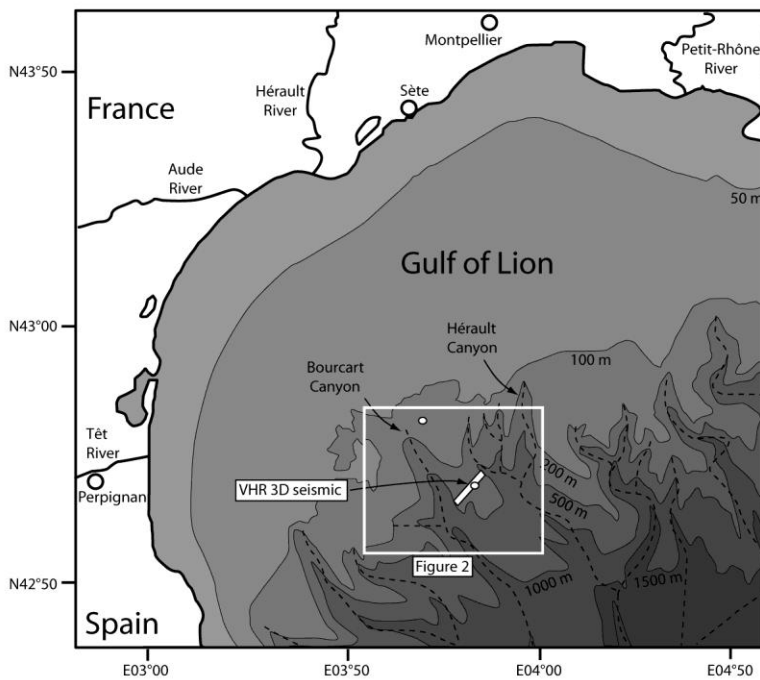
901 Zeppilli, D., Canals, M., Danovaro, R. 2012. [Pockmarks enhance deep-sea benthic biodiversity: a case](#)  
902 [study in the western Mediterranean Sea](#). *Diversity & Distributions*, Vol. 18: Issue 8, p. 832-846.

903

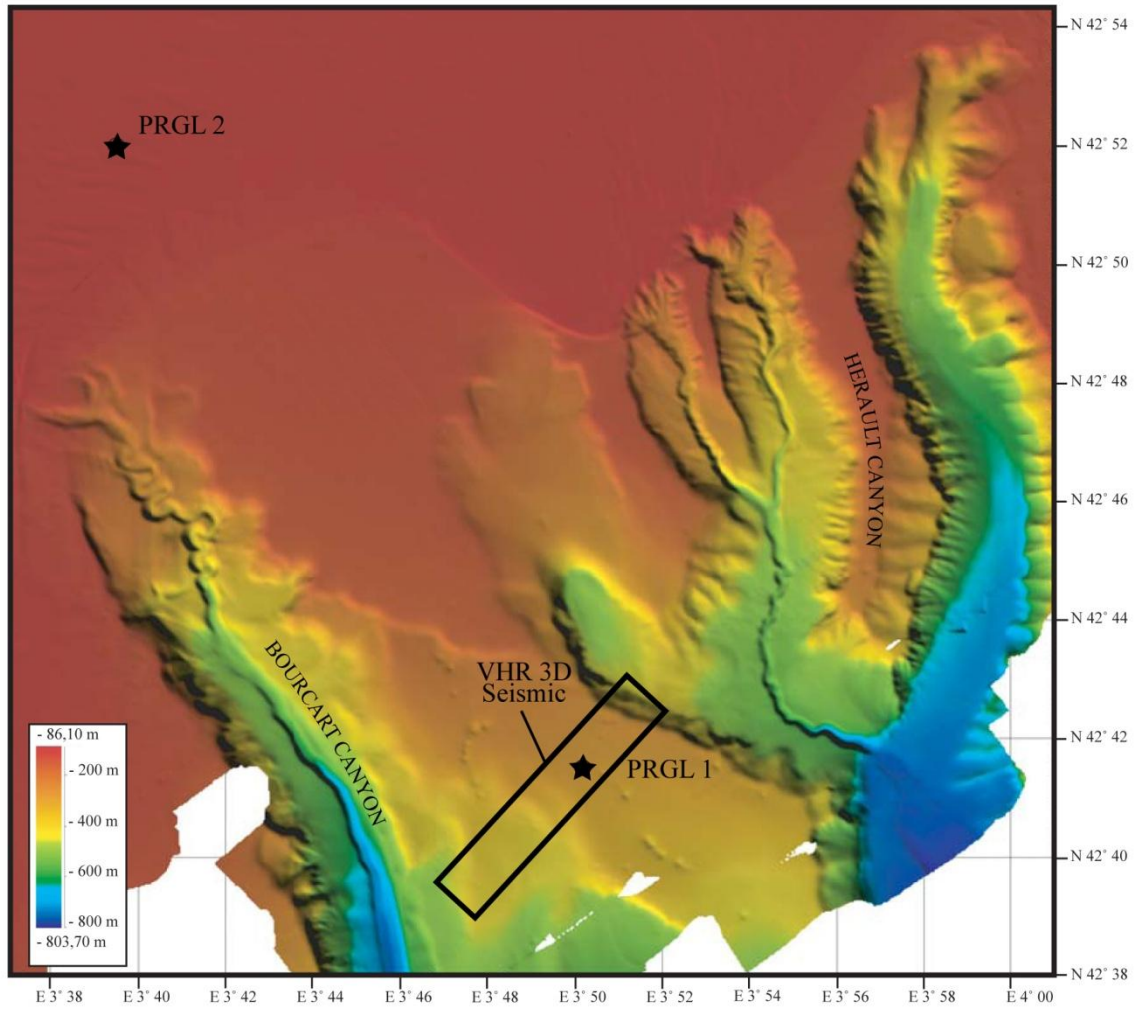
904

905

906



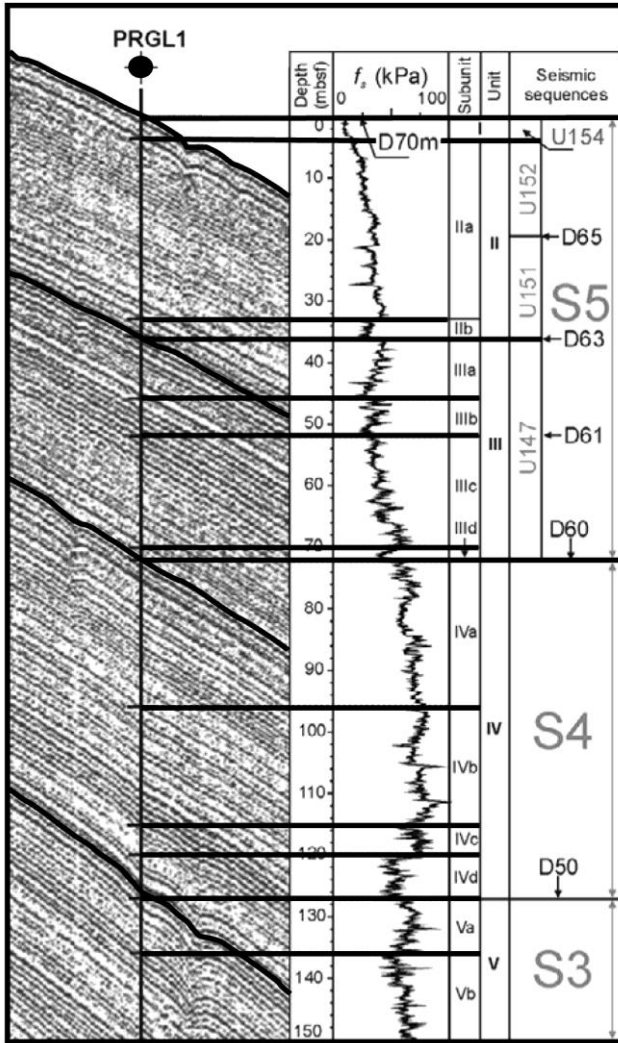
907  
908 Fig.1  
909



910

911 Fig. 2

912

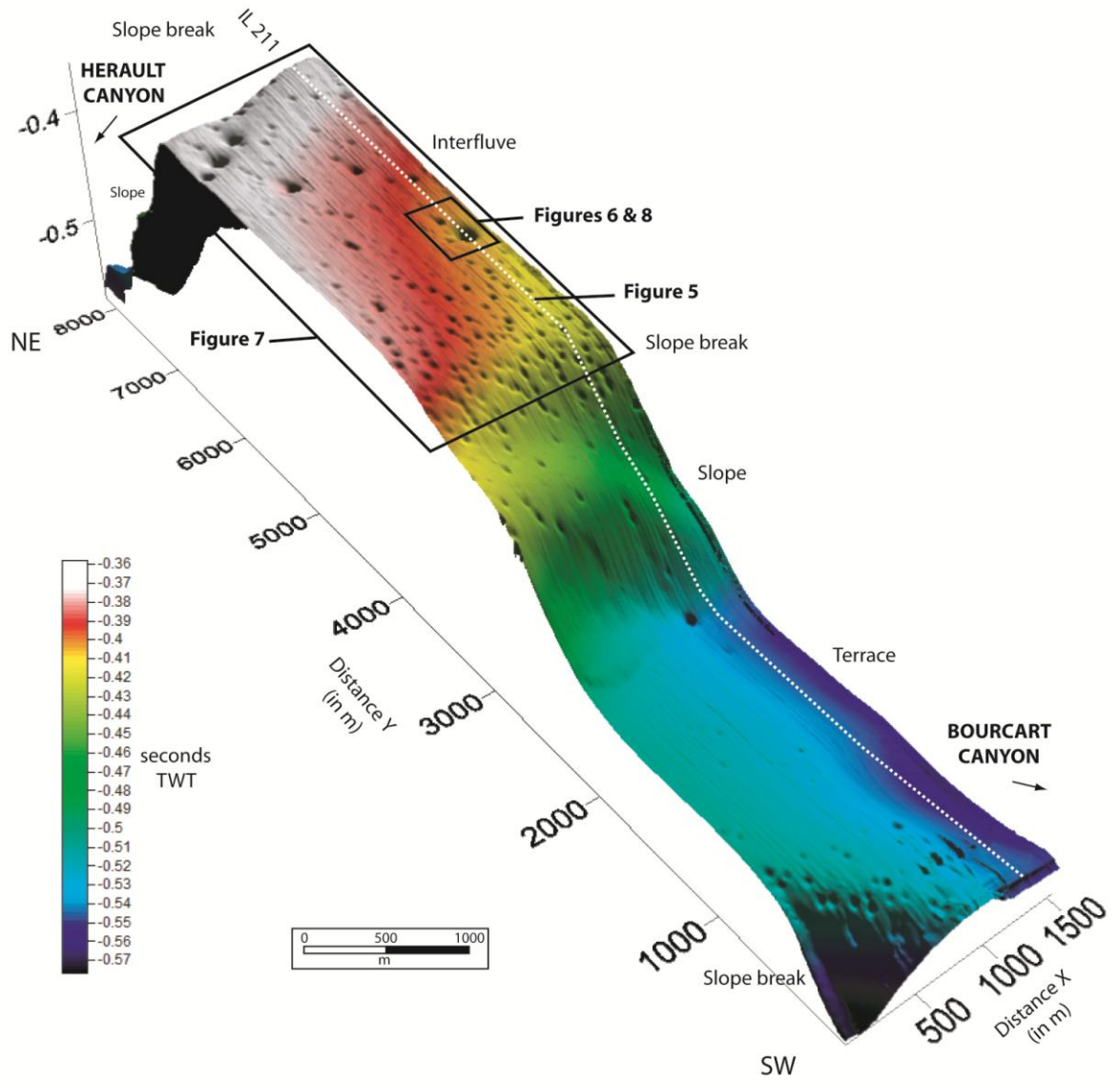


913

914 Fig. 3

915

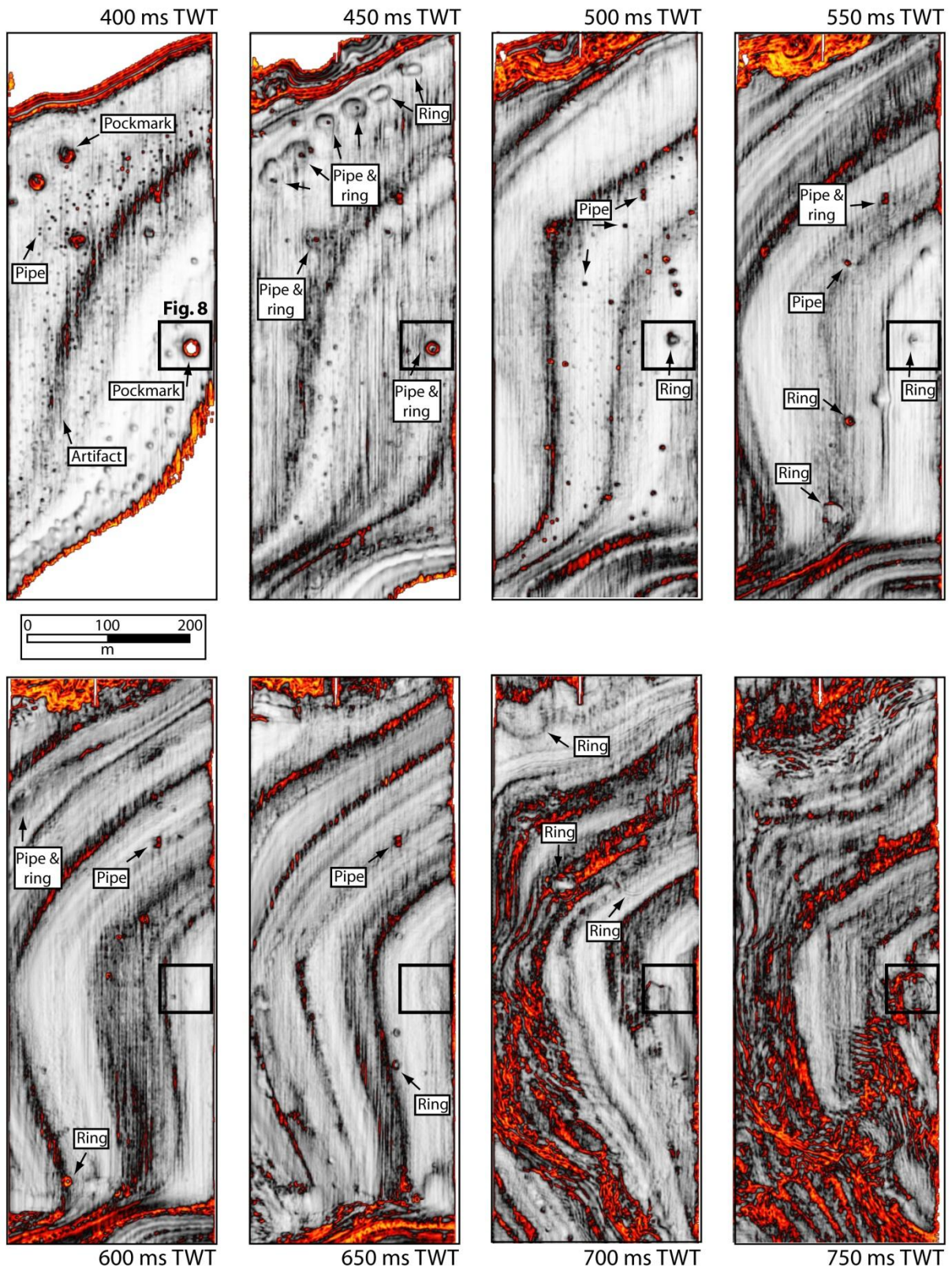




916  
917 Fig. 4  
918



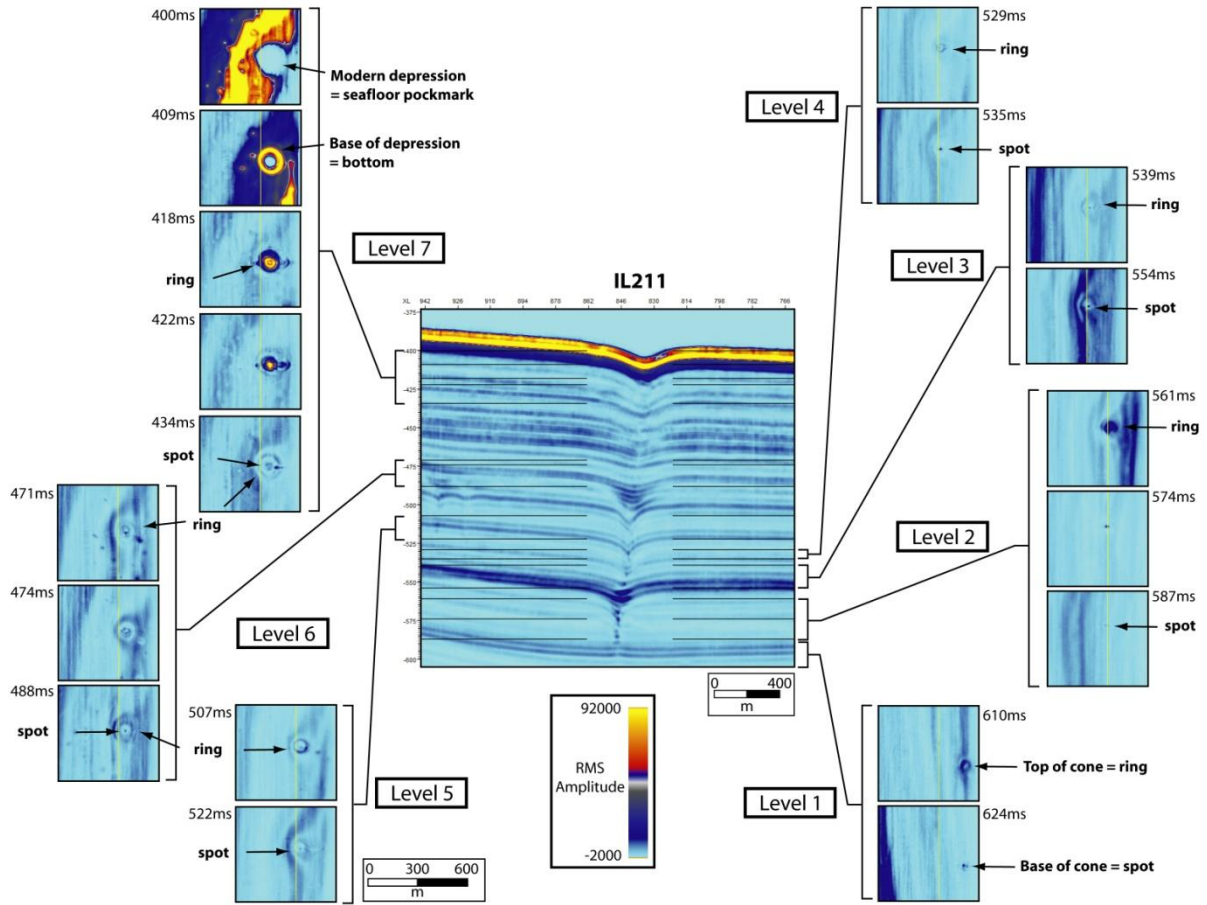




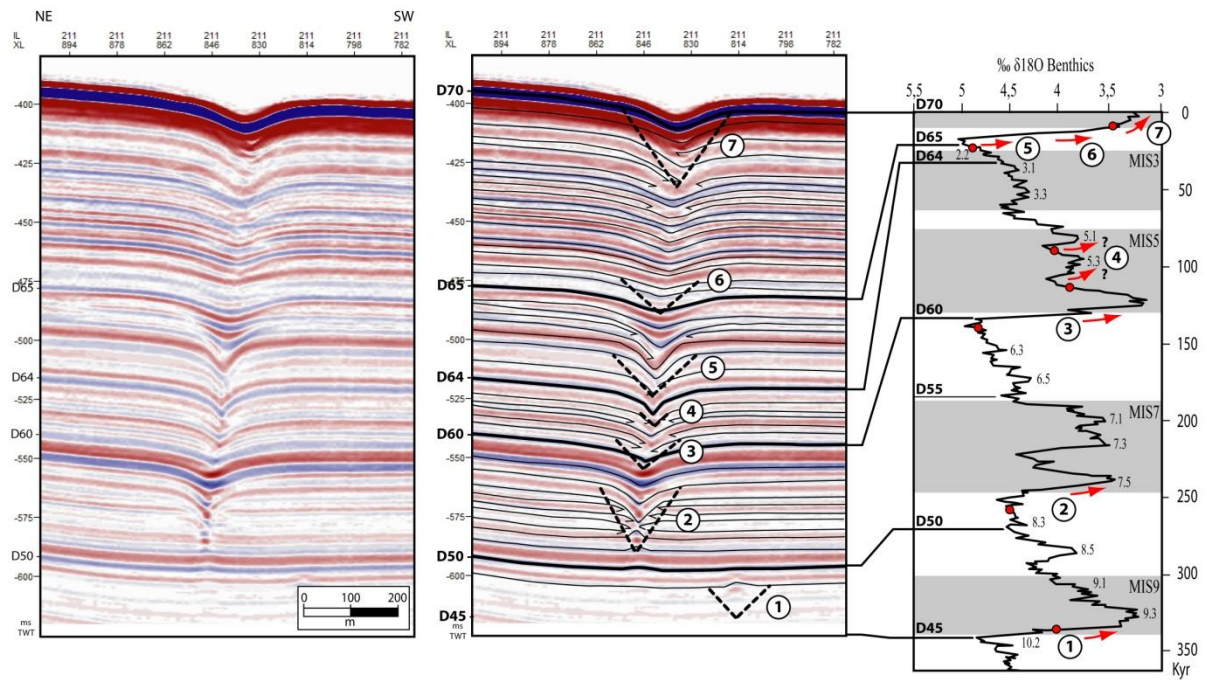
925

926 Fig. 7

927

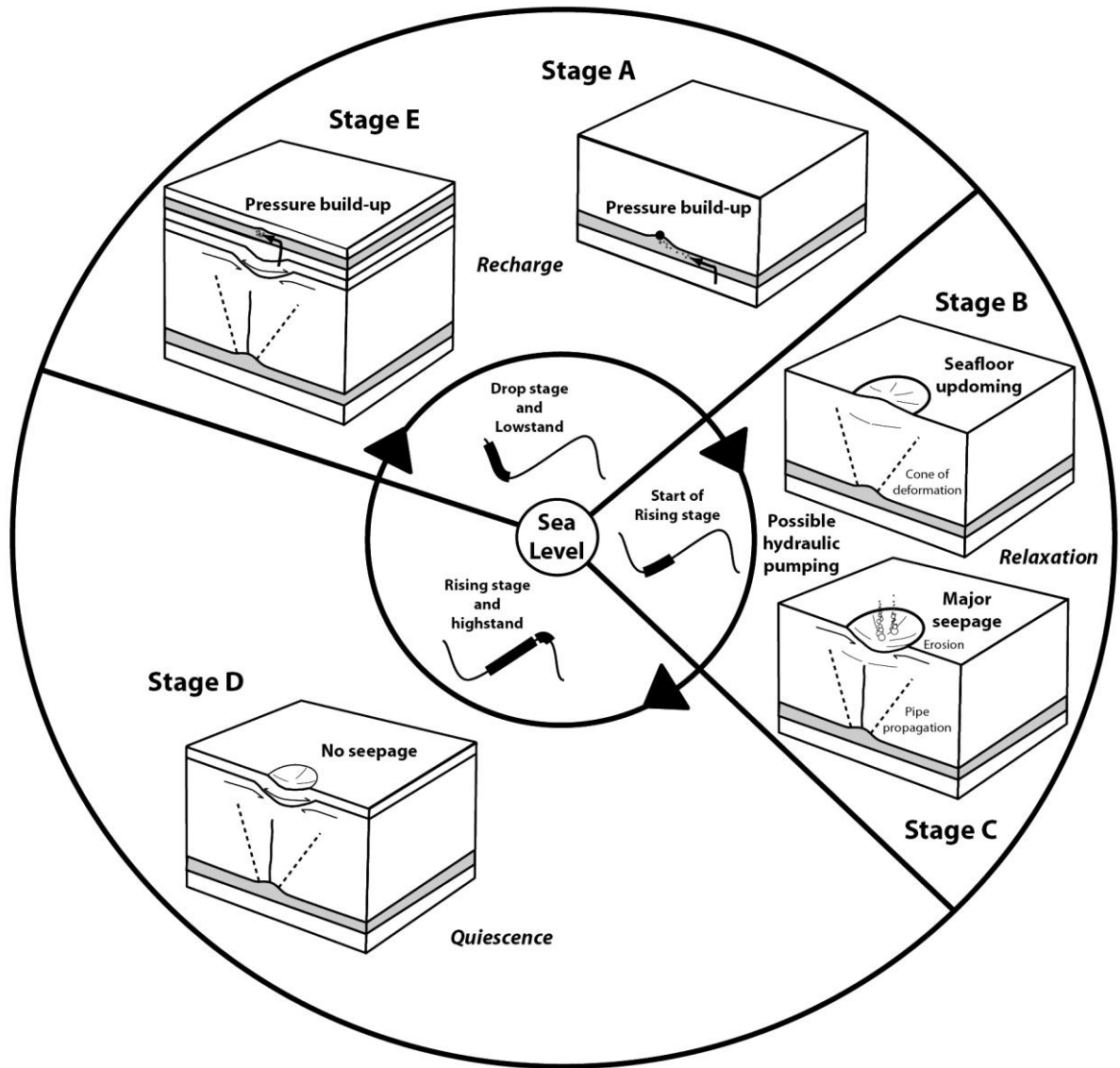


928  
929 Fig. 8  
930



931  
932 Fig. 9





933

934 Fig. 10